On the Leeuwin Current System and Its Linkage to Zonal Flows in the South Indian Ocean as Inferred from a Gridded Hydrography

RYO FURUE

Application Laboratory, JAMSTEC, Yokohama, Japan

KÉVIN GUERREIRO

LEGOS, Toulouse, France

HELEN E. PHILLIPS

IMAS, and ARC CSS, University of Tasmania, Hobart, Australia

JULIAN P. MCCREARY, JR.

IPRC, University of Hawaii, Honolulu, Hawaii

NATHANIEL L. BINDOFF

ARC CSS, and ACE CRC, and IMAS, University of Tasmania, and CSIRO, Hobart, Australia

(Manuscript received 20 July 2016, in final form 26 December 2016)

ABSTRACT

The Leeuwin Current System (LCS) along the coast of Western Australia consists of the poleward-flowing Leeuwin Current (LC), the equatorward-flowing Leeuwin Undercurrent (LUC), and neighboring flows in the south Indian Ocean (SIO). Using geostrophic currents obtained from a highly resolved ($^1/_8°$) hydrographic climatology [CSIRO Atlas of Regional Seas (CARS)], this study describes the spatial structure and annual variability of the LC, LUC, and SIO zonal currents, estimates their transports, and identifies linkages among them. In CARS, the LC is supplied partly by water from the tropics (an annual mean of 0.3 Sv; 1 Sv $\equiv 10^6$ m^3 s^{-1}) but mostly by shallow ($\lesssim$200 m) eastward flows in the SIO (4.7 Sv), and it loses water by downwelling across the bottom of this layer (3.4 Sv). The downwelling is so strong that, despite the large SIO inflow, the horizontal transport of the LC does not much increase to the south (from 0.3 Sv at 22°S to 1.5 Sv at 34°S). This LC transport is significantly smaller than previously reported. The LUC is supplied by water from south of Australia (0.2 Sv), by eastward inflow from the SIO south of 28°S (1.6 Sv), and by the downwelling from the LC (1.6 Sv) and in response strengthens northward, reaching a maximum near 28°S (3.4 Sv). North of 28°S it loses water by outflow into subsurface westward flow (−3.6 Sv between 28° and 22°S) and despite an additional downwelling from the LC (1.9 Sv), it decreases to the north (1.7 Sv at 22°S). The seasonality of the LUC is described for the first time.

1. Introduction

The Leeuwin Current System (LCS) along the coast of Western Australia (WA) consists of the Leeuwin Current (LC), the Leeuwin Undercurrent (LUC), and the nearshore Capes and Ningaloo Currents. It also includes the zonal flows in the south Indian Ocean (SIO) that impinge on the west coast of Australia: near-surface ($\lesssim$200 m) eastward flow and subsurface westward flow.

Denotes content that is immediately available upon publication as open access.

School of Ocean and Earth Science and Technology Publication Number 9882 and International Pacific Research Center Publication Number 1230.

Corresponding author e-mail: Ryo Furue, furue@hawaii.edu

DOI: 10.1175/JPO-D-16-0170.1

The LC and LUC are remarkable in that they flow poleward and equatorward, respectively, opposite to the directions of the boundary currents along most eastern-ocean boundaries in the Atlantic and Pacific Oceans (Cresswell and Golding 1980; Thompson 1984; Smith et al. 1991; Godfrey et al. 1995), the sole exception occurring off Portugal (Frouin et al. 1990). The near-surface eastward current is noteworthy because it flows against the predictions of wind-driven theory (Schott et al. 2009).

a. Background

At the present time, there are many studies of various aspects of the LCS. Here, we summarize a few that are most relevant to our research.

1) LEEUWIN CURRENT

Although the existence of near-surface, poleward flow off WA has been known for a century (Saville-Kent 1897), only in the latter half of the twentieth century has the LC been systematically observed. Smith et al. (1991) reported the seasonal variation of the LC at 29.5°S, finding that its transport in the upper 300 m was a minimum in February (1.4 Sv; $1\,\text{Sv} \equiv 10^6\,\text{m}^3\,\text{s}^{-1}$) and a maximum in June (6.8 Sv). Feng et al. (2003) studied the seasonal cycle of the LC at 32°S; they found that the LC meridional transport attained a maximum during June–July (5 Sv) and that its annual mean over the entire record was 3.4 Sv. More recently, Yit Sen Bull and van Sebille (2016) used Lagrangian virtual floats in their eddy-revolving ocean general circulation model (OGCM) to find annual-mean LC transport values similar to Feng et al.'s (2003).

Two mechanisms have been proposed for generating the LC. The first is the Indonesian Throughflow (ITF), which raises sea level north of Australia; the higher sea level extends southward along the WA coast through the propagation of coastally trapped waves, thereby establishing a zonal-pressure-gradient field that drives the LC (e.g., Godfrey and Ridgway 1985; Kundu and McCreary 1986). The second is near-surface, eastward flow across the interior of the SIO [section 1a(3)], which bends southward at the WA coast to form the LC (McCreary et al. 1986; Thompson 1987; Weaver and Middleton 1989, 1990; Furue et al. 2013; Benthuysen et al. 2014; Lambert et al. 2016). A general result from the second mechanism is that a southward-flowing LC can be produced, provided the onshore interior transport is large enough to overwhelm offshore Ekman drift driven by the prevailing southerly winds. This property holds in the SIO but generally not elsewhere (Weaver and Middleton 1990). Furthermore, the second mechanism suggests that the LC strengthens to the south as a consequence of the continual supply of water from the ocean interior.

It is noteworthy that steady currents exist at all along eastern-ocean boundaries; eastern boundary currents can occur only if some process prevents Rossby waves from propagating them offshore. The basic process that causes coastal trapping differs among the models. In the Kundu and McCreary (1986) and McCreary et al. (1986) models, coastal trapping results from vertical diffusion, which damps Rossby waves associated with higher-order vertical modes before they can propagate very far offshore. In the Weaver and Middleton (1989, 1990), Furue et al. (2013), and Benthuysen et al. (2014) solutions, it is caused by the continental slope, which traps Rossby waves to the coast by the topographic β effect.

An aspect of the LC, not captured in these idealized modeling studies, is that it is generally collocated with an energetic, mesoscale eddy field. Indeed, the LC is believed to generate eddies as a result of barotropic and baroclinic instabilities, which subsequently propagate offshore (Andrews 1983; Fang and Morrow 2003; Feng et al. 2005; Meuleners et al. 2007, 2008). As a result of the eddy field, the LC often appears as a meandering flow.

2) LEEUWIN UNDERCURRENT

Thompson (1984) first reported evidence for the LUC, noting the presence of equatorward flow on the upper continental slope off WA at a depth of 300 m and estimating its transport to be 5 Sv. Current meter data from the Leeuwin Current Interdisciplinary Experiment (LUCIE; Church et al. 1989; Smith et al. 1991) confirmed the Thompson (1984) observations, describing an equatorward undercurrent located between 250 and 400 m, flowing at a speed of about $10\,\text{cm}\,\text{s}^{-1}$ and transporting 5 Sv of high-salinity and highly oxygenated water. Middleton and Cirano (2002) suggested that the LUC is fed by the Flinders Current (Bye 1972), which flows westward along and slightly offshore of the South Australian shelf and transports Subantarctic Mode Water (SAMW). Analyses of the different water masses off WA (Akhir and Pattiaratchi 2006; Woo and Pattiaratchi 2008) confirmed that the LUC does carry SAMWs.

The dynamics of the LUC are not clear. The Kundu and McCreary (1986) and McCreary et al. (1986) models are appealing in that they generate the LUC (indeed, the complete LCS) within a simple theoretical framework. In both, the LUC and LC are composed of damped, baroclinic Rossby waves. As a result, the two currents are strongly connected dynamically. For example, water downwells from the LC to the LUC because of damping, providing the source for all the LUC water. Finally,

the LUC is linked to the westward, subsurface flows in the interior of the SIO, with LUC water diverging from the coast to supply water for the westward SIO flow. One limitation of the two models is that they lack a continental shelf, which is known to weaken (inhibit) offshore Rossby-wave propagation (Weaver and Middleton 1990; Furue et al. 2013; Benthuysen et al. 2014), and without shelf topography, the model LC and LUC are necessarily aligned vertically with equal and opposite transports, whereas the real LUC tends to be shifted offshore. Another limitation is that, unless diffusion is sufficiently strong (perhaps unrealistically so), both the LC and LUC are weak and the LUC does not extend deep enough into the water column. Given these issues, it is best to view the two modeling studies as providing a useful foundation for a hierarchy of LUC systems.

Some OGCMs develop a LUC with a realistic structure and amplitude (e.g., Domingues et al. 2007; Meuleners et al. 2007). Domingues et al. (2007) examined LUC flow pathways in their solution. Similar to the Kundu and McCreary (1986) and McCreary et al. (1986) solutions, they report that LC water sinks to join the LUC and eventually bends offshore to join the SIO subsurface westward flow. In contrast to those solutions, however, the downwelling appears to occur mostly isopycnally, rather than diffusively; as LC water flows southward, it cools and sinks to merge with the top of the LUC (C. M. Domingues 2014, personal communication). In addition, the LUC and LC do not align vertically, likely a consequence of their model having a continental shelf/slope.

Although the eddy field associated with the LUC is thought to be energetic, it is not readily observed. In a ROMS simulation, Rennie et al. (2007) found that the LUC generated mostly cyclonic eddies due to the production of strong negative vorticity where the current flowed against the continental slope. They also found that interaction between the LC and LUC led to the formation of eddy pairs: cyclonic in the LUC and surface-intensified, anticyclonic eddies in the LC. Meuleners et al. (2007) found LUC variability to be coupled to the more energetic LC variability, with the development of LC meanders leading to the growth of subsurface eddies.

3) SIO ZONAL CURRENTS

The upper-ocean (shallower than 200–300 m) circulation of the SIO is dominated by geostrophic eastward currents that flow against the prevailing winds (Schott et al. 2009). The cause of the eastward flow appears to be the poleward increase in density, which results in a poleward decrease of near-surface dynamic height. As a result, the near-surface geopotential height field offshore from WA nearly always decreases toward the south (Thompson 1984; McCreary et al. 1986; Woo and Pattiaratchi 2008), driving a continual input of water into the coast. In addition, the eastward flow tends to split into a number of jets (Maximenko et al. 2009; Divakaran and Brassington 2011), the most distinctive of which are the tropical Eastern Gyral Current (EGC), which reaches the eastern boundary from 15° to 20°S (Meyers et al. 1995; Domingues et al. 2007; Menezes et al. 2013), and the South Indian Countercurrent (SICC; Siedler et al. 2006; Palastanga et al. 2007), which appears to divide into two branches near 25° and 30°S near the WA coast (Menezes et al. 2014).

SIO subsurface flow (deeper than 200–300 m) is directed predominantly westward. Sufficiently far offshore, westward flow exists as part of the wind-driven Sverdrup gyre, but its cause near the WA coast is not understood. In the Kundu and McCreary (1986) and McCreary et al. (1986) models, it is generated by the offshore propagation of weakly damped, low-vertical-mode Rossby waves and hence is determined by LCS processes. In OGCMs with a continental shelf/slope, for which Rossby-wave propagation is inhibited, this mechanism is likely to be significantly modified. As for the overlying eastward flow, the westward flow also tends to organize into jets, and such jets are visible in OGCM solutions (e.g., Domingues et al. 2007; Divakaran and Brassington 2011). The cause of westward jets is not clear but is likely linked to that of the overlying eastward ones.

b. *Present research*

In this study, we continue the effort to develop a comprehensive, observational picture of the LCS for both its annual-mean state and seasonal variability. We seek to answer questions like the following: What are the spatial and temporal structures of the LC and LUC? How do their transports vary along the coast? Is there significant downwelling from the LC to the LUC? How do the two coastal currents interact with the SIO zonal flows? To address these questions, we analyze hydrographic data from a recently updated variant of the CSIRO Atlas of Regional Seas (CARS), a climatology with sufficient spatial resolution (1/8°) to represent the narrow coastal currents along WA. On the basis of geostrophic currents determined from CARS, we describe the spatial structure and annual variability of the LC, LUC, and SIO zonal currents, estimate their transports, and identify linkages among them. We use two methods to determine the currents: (i) by imposing a level of no motion offshore and a zero alongshore flow on the shelf/slope (Helland-Hansen 1934) and (ii) by

imposing zero depth-integrated divergence at a specified level offshore as well as on the shelf/slope. To support our CARS analyses, at various places in the text we report properties of the LCS in an OGCM solution, namely, the Ocean Forecasting Australian Model 3 (OFAM3; Oke et al. 2013).

We find that the observed circulation off WA has many similarities to the circulation described in the earlier modeling studies reviewed above. In particular, the LC is fed by near-surface eastward flow, water downwells from the LC to the LUC, and the LUC loses water to subsurface westward flow. Surprisingly, the downwelling transport is large, a significant fraction of the eastward zonal transport, and as a result the LC transport does not increase much to the south, in contrast to a number of modeling results.

The paper is organized as follows. Section 2 provides an overview of CARS and OFAM3 and discusses the methods of analysis, and section 3 describes the alongshore structure and seasonal variability of the LC, LUC, and SIO flows present in CARS and identifies the linkages among them. Section 4 provides a summary and discussion, and, finally, the appendix discusses supplementary results from OFAM3 and another eddy-resolving model called the OGCM for the Earth Simulator (OFES).

2. Methodology

We begin with a discussion of the observational data and OGCM solution that we use in our study. We then discuss our two methods for calculating geostrophic currents and validate both approaches by applying them to the OGCM solution. Finally, we define spatial boundaries for the LC and LUC and use them to provide expressions for the current transports reported in section 3.

a. Data

Hydrographic data are taken from a version of the CSIRO Atlas of Regional Seas that has high resolution around Australia (CARS Aus8; Ridgway et al. 2002; Dunn and Ridgway 2002; http://www.cmar.csiro.au/cars/; http://www.marine.csiro.au/atlas/). The atlas provides the mean and average annual cycle of hydrographic measurements obtained by research vessels and Argo and other autonomous profiling buoys from 1950 to the end of 2012. Data are provided on a grid with a resolution of 1/8° and with 79 vertical levels spread over 5500 m, 55 of which are within the top 1000 m. CARS differs from other climatologies through its use of an adaptive length-scale LOESS mapper that maximizes the resolution in data-rich regions. The nominal effective resolution of the original hydrographic measurements is roughly 100 km for the region and depth range we are interested in, but the effective resolution is highly anisotropic near the coast with data ellipses tending to align along isobaths and elongated in the alongshore direction (Ridgway et al. 2002). Accordingly, the temperature (T) or salinity (S) value at each grid point is a result of averaging (smoothing) over many observed data, and the effective smoothing scale is smaller in the cross-shore direction than in the alongshore direction, a crucial property to resolve narrow alongshore currents. The values are deliberately extended beneath the sloping bottom so that the user can choose various bottom masks without creating gaps between the data points and the ocean bottom. In this study, we mask the CARS data using the ETOPO5 topography dataset (National Geographical Data Center 1988). At a 1/12° resolution, ETOPO5 requires only simple linear interpolation onto the 1/8° CARS grid.

Even though the effective resolution is higher in the cross-shore direction, it will still be lower than the grid resolution (1/8°) of CARS Aus8 (K. R. Ridgway 2016, personal communication). A coarser grid, however, would have undersampled the spatial structure of the interpolator (smoother) function near the coast, smoothing out the narrow alongshore currents, and it also would have required horizontal interpolation after all to resolve steep bottom topography. It is this high horizontal and vertical resolution that makes this atlas particularly useful because a major potential source of error comes from the application of mass conservation to the sloping bottom [sections 2c(2) and 3d]. Here, we analyze a regional subset of the dataset that extends north, west, and south of the continental boundary of Australia from 40° to 16°S and 90° to 120°E.

To calculate the near-surface, onshore–offshore transport into the LCS, we need to take into account the wind-driven Ekman drift away from the coast. When analyzing the CARS data, we use monthly climatological winds over 2002–11 constructed from ERA-Interim (Dee et al. 2011). [The selection of years 2002–11 is not particularly significant. The only consideration was that the hydrographic observations that went into the revised CARS Aus8 dataset are biased toward the recent Argo era. We have compared the ERA-Interim zonal and meridional winds averaged over 2002–11 to those over 1992–2001 in our region of interest and found only up to ~5% difference (not shown).] When carrying out the same analysis on the OFAM3 temperature and salinity fields [section 2c(3)], we use the wind stress data that forced OFAM3 (also based on ERA-Interim; see below), which is provided as part of the OFAM3 dataset (section 2b).

b. Model

To validate our geostrophic calculations (section 2c), we utilize a solution from OFAM3 (Oke et al. 2013). OFAM3 is a near-global (75°S to 75°N), eddy-resolving configuration of version 4.1d of the Modular Ocean Model (Griffies 2009). Its horizontal resolution is 1/10°, and it has 51 vertical levels, with 5-m resolution from the surface to 40 m, 10-m resolution from 40 to 200 m, and an increasing grid step at deeper levels. The model is initialized with potential temperature and salinity from the global version of CARS (1/2°, CARS2009; Ridgway and Dunn 2003) and is forced by 3-hourly surface fluxes of heat, freshwater, and momentum from the ERA-Interim product (Dee et al. 2011) for the period 1993–2005. In addition, surface temperature is restored to monthly averaged observations (Reynolds SST; Reynolds et al. 2007) with a nominal restoring time scale of 10 days for the 5-m-thick, topmost model layer. Similarly, surface salinity is restored to a monthly averaged climatology (CARS2009) with a restoring time scale of 30 days. We use the monthly climatology of this integration.

c. Geostrophic velocity fields

1) HELLAND-HANSEN (1934) METHOD

Helland-Hansen (1934, hereinafter HH) introduced a popular method for determining geostrophic velocities in a hydrographic section that extends over a shelf/slope [see Sælen (1959), Mountain (1974), Fratantoni and Pickart (2007), and Bingham and Hughes (2012) for more recent discussions]. Offshore, the HH method assumes a level of no motion at some depth d_0. Near the coast, where the bottom depth $D(x, y)$ is shallower than d_0, it assumes that the alongshore velocity vanishes at $z = -D$.

When the HH method is applied to the CARS dataset, which is essentially a suite of cross-shore (zonal) hydrographic sections, the cross-shore velocity is also assumed to vanish at $z = -D$. See Bingham and Hughes (2012) for a comprehensive assessment of this and other similar methods. We label the geostrophic flow field determined from CARS by the HH method $\mathbf{v}_g = (u_g, v_g)$.

2) ZERO DIVERGENCE METHOD

A limitation of the HH method is that it allows flow across the bottom of the shelf/slope, a property that is problematic when determining volume budgets (section 3d). It is possible to add a barotropic velocity field to $\mathbf{v}_g$ that eliminates this deficiency. Let $d_b(x, y) = \min[d_0, D(x, y)]$, that is, d_b is the reference level d_0 offshore and D on the shelf/slope. Then, the flow across d_b driven by the HH geostrophic currents is $\nabla \cdot \mathbf{V}$, where

$$\mathbf{V} \equiv \int_{-d_b}^{0} \mathbf{v}_g \, dz - \mathbf{k} \times \frac{\boldsymbol{\tau}}{f\rho_o}, \tag{1}$$

$\boldsymbol{\tau} = (\tau^x, \tau^y)$ is wind stress, ρ_o is a constant mean density, and $\mathbf{k}$ is an upward-pointing unit vector. To eliminate any across-bottom flow, we use a Helmholtz decomposition; that is, we subtract a rotationless, depth-integrated velocity field $\nabla\phi(x, y)$ from $\mathbf{V}$ such that $\nabla \cdot (\mathbf{V} - \nabla\phi) = 0$, so that ϕ satisfies the Poisson equation

$$\nabla^2\phi = \nabla \cdot \mathbf{V}. \tag{2}$$

We solve (2) subject to the condition that there is no flow through the domain boundaries except for the western boundary by setting $\phi_n = 0$ there, where the subscript n designates a derivative normal to the boundary. Since the total convergence/divergence of the original velocity field, $\int \nabla \cdot \mathbf{V} \, dx \, dy$, is nonzero in general, the correction velocity $\nabla\phi(x, y)$ must have a net inflow or outflow across the lateral boundary to cancel out $\int \nabla \cdot \mathbf{V} \, dx \, dy$. We choose to allow for such a flow only across the western boundary by setting $\phi = 0$ there, because it is far from our region of interest and the impacts of this weak artificial flow will be minimal.

The geostrophic flow field using this method is then given by $\mathbf{v}'_g \equiv \mathbf{v}_g - (\nabla\phi)/d_b$. We refer to this approach as the zero divergence (ZD) method, as it results in a flow field that satisfies $\nabla \cdot \left[\int_{-d_b}^{0} \mathbf{v}'_g \, dz - \mathbf{k} \times \boldsymbol{\tau}/(f\rho_o)\right] = 0$ everywhere, offshore as well as on the shelf/slope.

Marchuk et al. (1973) and Sheng and Thompson (1996) propose more dynamically consistent methods of determining from an observed density field a velocity field that does not have across-bottom flow. Both methods include friction. We use the above alternative only because it is much simpler to implement.

3) VALIDATION

We checked the accuracy of the HH and ZD methods using the OFAM3 solution. Specifically, we used the climatological temperature and salinity fields from the model output (section 2b) to determine annual-mean, meridional velocities v_g and v'_g and compared them with the model's absolute climatological v. Figure 1 plots zonal sections of differences (shading) between annual-mean velocities at 30°S: between v (contours) and v_g with $d_0 = 300$ m (left) and 900 m (center) and between v and v'_g with $d_0 = 900$ m (right). There are large near-surface differences ($z > -30$ m), owing to the lack of the Ekman layer in the geostrophic calculations. Below the

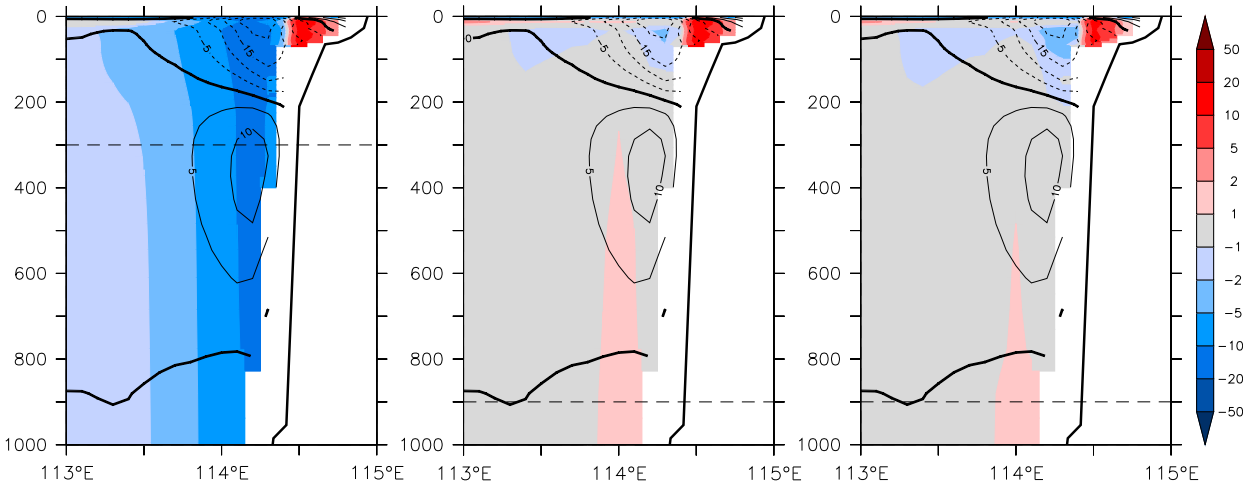

FIG. 1. Zonal sections from OFAM3 of annual-mean, velocity differences (cm s^{-1}; shading), showing $v_g - v$ with (left) $d_0 = 300$ m and (center) $d_0 = 900$ m and (right) $v'_g - v$ with $d_0 = 900$ m at 30°S. Notice the logarithm-like color intervals. Absolute velocity v is contoured with positive (negative) values indicated by solid (dashed) curves. The contour interval is 5 cm s^{-1}. The bottom topography is from the ETOPO5 dataset (National Geographical Data Center 1988).

Ekman layer, velocity differences tend to be much smaller for $d_0 = 900$ m except on the slope/shelf, where the difference is up to ~10 cm s^{-1} and does not change much between the three panels. The good agreement when $d_0 = 900$ m (with similar results at other latitudes) supports the use of the HH and ZD methods to determine the alongshore flow field.

Figure 1 points toward a large difference in the LC and LUC strengths depending on the reference level d_0. The upper panels of Fig. 2 illustrate this sensitivity in greater detail, plotting LC and LUC transports $\mathcal{V}_{\rm LC}$ and $\mathcal{V}_{\rm LUC}$ from OFAM3 at 30°S versus d_0, where $\mathcal{V}_{\rm LC}$ and $\mathcal{V}_{\rm LUC}$ are defined below in (4a) and (6a). The transports change markedly as d_0 increases from 300 to 1000 m for both the HH (solid) and ZD (dashed) methods, attaining a minimum or maximum when $d_0 \approx$ 1000 m. The large variation happens because the presence of the LUC ensures that the reference-level velocity is not small for values of d_0 smaller than 1000 m. Indeed, the maximum discrepancy in Fig. 2 occurs for $d_0 = 300$–400 m, the depths where the LUC attains its maximum speed (Fig. 1). Note that $d_0 = 200$ m appears to be another good choice, given the separation between the LC and LUC being at about 200 m (Fig. 1, contours); however, we opt not to do so because the offshore flow field includes much deeper structures (see below).

For $d_0 \gtrsim 1000$ m, the transports slowly increase or decrease. Visual inspection indicates that the v field from the geostrophic calculation starts to compare less well to the absolute velocity field of OFAM3 as d_0 is increased beyond 1000 m. The cause of this change appears to be ageostrophy at the deep sloping bottom. The actual vertical shear of the OFAM3 absolute velocity there is significantly different from the geostrophic shear predicted from horizontal density gradients. This spurious shear affects the calculated geostrophic velocity well above the bottom (not shown). This ageostrophy could be due to bottom friction but details are not known.

These characteristics generally hold for other latitudes. That is, the separation between the LC and LUC is at about 200 m in OFAM3; the LC and LUC transports reach their minimum and maximum when $d_0 = 800$–1000 m, where they agree best with the transports calculated from the full model velocity, and the flow field starts to deteriorate for deeper reference levels. Figures 2c and 2d plot $\mathcal{V}_{\rm LC}$ and $\mathcal{V}_{\rm LUC}$ for $d_0 =$ 900 m, which is the overall best reference level that brings the geostrophic calculation of $\mathcal{V}_{\rm LC}$ and $\mathcal{V}_{\rm LUC}$ closest to the full model transports. We have visually compared various zonal sections of v_g and v'_g from CARS to those from OFAM3 and found that the dependency of the geostrophic flow pattern from CARS on d_0 is generally similar to that from OFAM3. The dependency of the LC and LUC transports from CARS on d_0 is also similar: they increase with increasing d_0 up to ~1000 m and flatten out or start to decrease beyond it not only at this latitude (black curves in Figs. 2a and 2b) but also at other latitudes in general (not shown). Unless specified otherwise, therefore, all geostrophic velocities reported below are determined using $d_0 = 900$ m.

As the gray curves in Figs. 2c and 2d indicate, the ZD method usually gives somewhat larger (smaller) LC (LUC) transports, and the difference tends to be larger

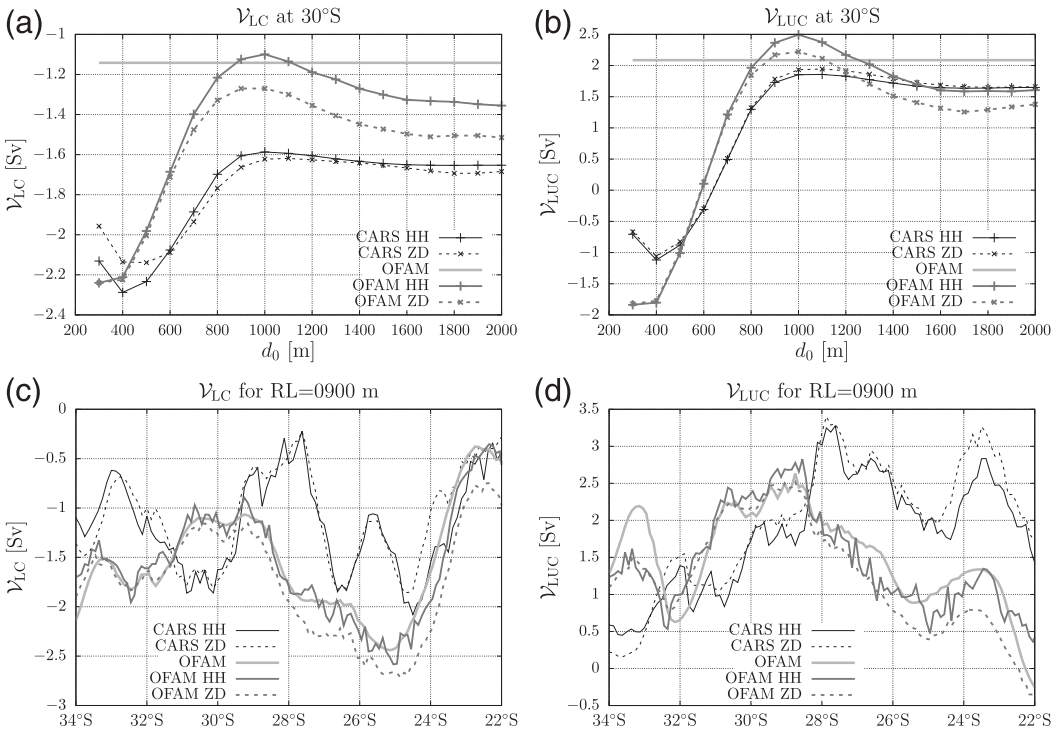

FIG. 2. Annual-mean transports of (a) the LC and (b) the LUC at 30°S vs reference depth d_0 and (c),(d) those for $d_0 = 900$ m vs latitude, using the CARS (black) and OFAM3 (gray) annual-mean T–S fields and determined by the HH (solid) and ZD (dashed) methods. The LC transports include Ekman transports. The thick, gray curve shows the transport based on the OFAM3 velocity field.

north of 28°S; the discrepancy between the geostrophic calculation and the full model velocity is also somewhat larger north of 28°S. The ZD correction is nevertheless necessary for our study because the spurious, net vertical transport across the bottom in the HH velocity field is not negligible in the volume budget calculations we show in section 3d. Interestingly, the ZD curves are much smoother than HH curves, consistent with the fact (not shown) that small scales dominate the horizontal divergence of the HH velocity field, and eliminating it involves horizontal smoothing, a property of the Poisson equation [(2)]. The difference between the HH and ZD methods for the LC transport from CARS (black curves in Fig. 2c) is somewhat smaller than that from OFAM3 except between 24.5° and 23°S; for the LUC transport (Fig. 2d), the difference is similar between OFAM3 and CARS. (The interested reader can find some further comparison between the CARS and OFAM3 flow field in the appendix.)

d. Transports

There are distinct advantages in having a coordinate system that approximately follows the currents. There is, however, no perfect way to define current boundaries. One problem is that the boundaries of these currents are highly variable in space and time. We define the boundaries to be constant in time on the basis of the annual-mean climatological flow structure, which is smoother also in space than monthly climatology. Another problem is that the definitions of the LC and LUC are somewhat ambiguous. Past studies tend to show a well-defined LC core trapped to the continental slope. Sometimes, however, offshore flow is in the same direction as the LC (e.g., Smith et al. 1991), and it is not clear whether or not this flow should be included in the LC. The spatial structure of the LUC is less well documented, but the same problem is anticipated. In this study, we define the LC and LUC to be the cores that are trapped to the continental slope for two reasons: that they are almost always well defined (see below) and that the cores trapped to the slope or coast are likely to be dynamically separate phenomena from offshore currents (section 1a).

Since the vertical structure of the LC is relatively constant in the latitudinal direction, we assume that the bottom of the LC occurs at the depth $d_{LC}(x, y) = \min[d_1, D(x, y)]$, that is, it is d_1 offshore and D over the shelf/slope, and set $d_1 = 200$ m. We set the depths of the top of the LUC to be d_{LC} and its bottom to be $d_b(x, y)$ [defined in section 2c(2)] for simplicity. The eastern

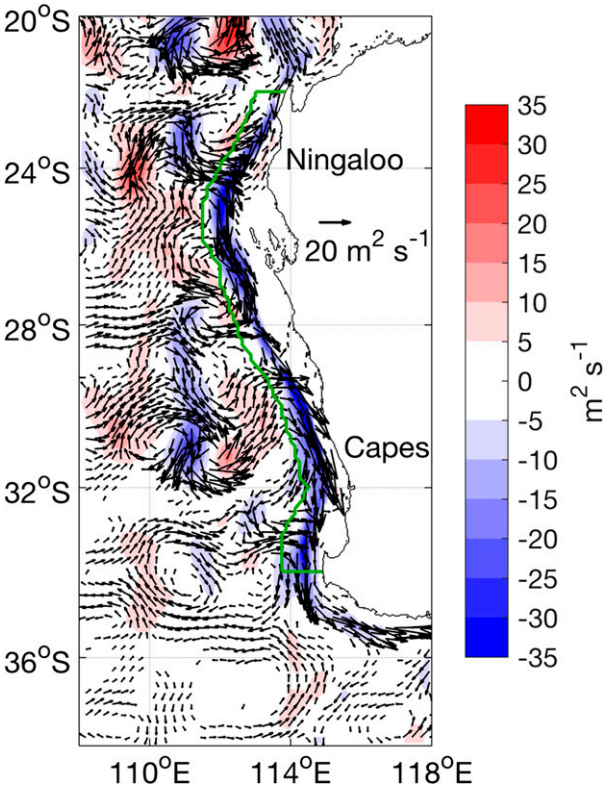

FIG. 3. Map of annual-mean, geostrophic velocities $\mathbf{v}_g'$ integrated from $z = -200$ m to the surface (arrows), with its meridional component $\int v_g' \, dz$ shaded ($m^2 s^{-1}$). The green line is $x_{LC}(y)$ and the northern and southern edges of the LC box (section 2d). The text on Australia indicates the locations where the observed Ningaloo and Capes Currents appear in summer (Cresswell et al. 1989; Pearce and Pattiaratchi 1999; Woo et al. 2006).

edge of the LCS, $x_{WA}(y)$, is the coast of Western Australia.

The offshore edges of the LC and LUC can be likewise defined on the basis of the flow structure. We tried but eventually abandoned this approach because any criteria we devised either excluded some parts of the LC or LUC or included some non-LC or non-LUC offshore flows. We then decided to use the bathymetry since the LC and LUC tend to be aligned with it. This approach is not perfect either but is much simpler. The offshore edge of the LC $[x_{LC}(y)]$ is defined to be the grid point closest to the longitude that is 0.8° offshore from the location where the d_1 isobath intersects the shelf/slope; similarly, the offshore edge of the LUC $[x_{LUC}(y)]$ is the grid point approximately 0.8° offshore from where the 800-m isobath intersects the shelf/slope. The position of the slope is determined on the basis of the ETOPO5 topography dataset interpolated onto the CARS grid. We have settled on these offshore edges by visually inspecting the annual-mean meridional geostrophic velocity field based on CARS along various zonal sections so that x_{LC} and x_{LUC} visually agree with the actual edges of the LC and LUC as well as possible. The green lines in Figs. 3, 4, and 7 (shown below) indicate the locations of these boundaries. As these figures show, the boundaries generally fit the LC and LUC tightly and exclude offshore recirculations.

The boundaries define boxes that contain the LC and LUC, and all the transport values reported in section 3 are evaluated across their faces. (We tested alternative, more complicated, boundary definitions, finding that transport values are usually not much changed and that our main conclusions are unaffected.) For the LC box, let

$$\mathbf{V}_{LC}(x,y,t) \equiv \int_{-d_{LC}}^{0} \mathbf{v}_g \, dz - \mathbf{k} \times \frac{\boldsymbol{\tau}}{f\rho_o}. \tag{3}$$

Then, the transports across the southern, offshore, and bottom faces are

$$\mathcal{V}_{LC}(y,t) \equiv \int_{x_{LC}(y)}^{x_{WA}(y)} dx \, V_{LC}, \tag{4a}$$

$$\mathcal{U}_{LC}(y,t) \equiv \int_{y}^{y_n} dl \, \mathbf{n} \cdot \mathbf{V}_{LC}, \quad \text{and} \tag{4b}$$

$$\mathcal{W}_{LC}(y,t) \equiv \int_{y}^{y_n} dy' \int_{x_{LC}(y')}^{x_{WA}(y')} dx \, w^*_{LC}, \tag{4c}$$

where $w^*_{LC} \equiv -\nabla \cdot \mathbf{V}_{LC}$ is the volume transport (per horizontal area) across the surface $z = -d_{LC}$. In (4b), $\mathcal{U}_{LC}$ is determined by a contour integration along $x_{LC}(y)$, $\mathbf{n}$ is an inward-pointing unit vector perpendicular to $x_{LC}(y)$, and $y_n = 22°S$ is the latitude of the northern boundary of the analysis domain. Note that with these definitions, both $\mathcal{U}_{LC}$ and $\mathcal{W}_{LC}$ vanish at the northern boundary $y = y_n$, allowing them to be interpreted as a cumulative source or sink for the LC transport from y_n to y. Specifically, integrating the equation of continuity $u_x + v_y + w_z = 0$ over the LC box yields

$$-\mathcal{V}_{LC}(y,t) - [-\mathcal{V}_{LC}(y_n,t)] = \mathcal{U}_{LC}(y,t) + \mathcal{W}_{LC}(y,t), \tag{4d}$$

indicating that the southward increase in the LC transport is balanced by the inflow from the sidewall $x_{LC}(y)$ and the upwelling across the bottom of the box.

Similarly, for the LUC box, let

$$\mathbf{V}_{LUC}(x,y,t) \equiv \int_{-d_b}^{-d_{LC}} \mathbf{v}_g \, dz, \tag{5}$$

in which case, the transports across the northern, offshore, top, and bottom faces are

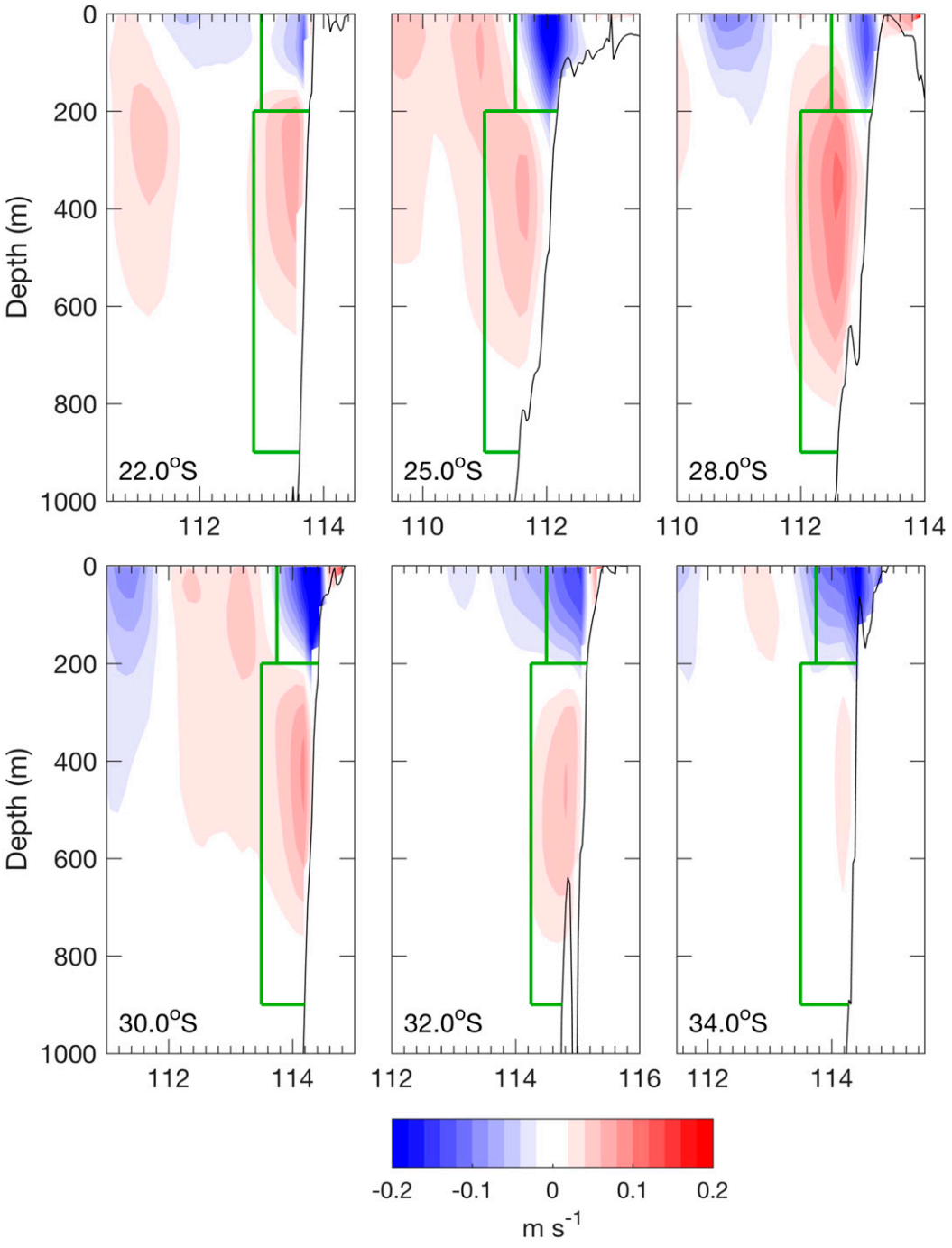

FIG. 4. Zonal sections of annual-mean, meridional, geostrophic velocities v_g' (m s^{-1}) at various latitudes. The vertical lines are the offshore boundaries of the LC and LUC, $x_{\mathrm{LC}}(y)$ and $x_{\mathrm{LUC}}(y)$, and the horizontal ones are the bottoms of the LC and LUC, d_1 and d_0 (section 2d).

$$\mathcal{V}_{\mathrm{LUC}}(y,t) \equiv \int_{x_{\mathrm{LUC}}(y)}^{x_{\mathrm{WA}}(y)} dx\, V_{\mathrm{LUC}}, \tag{6a}$$

$$\mathcal{U}_{\mathrm{LUC}}(y,t) \equiv \int_{y_s}^{y} dl\, \mathbf{n}\cdot\mathbf{V}_{\mathrm{LUC}}, \tag{6b}$$

$$\mathcal{W}_{\mathrm{LUC}}(y,t) \equiv \int_{y_s}^{y} dy' \int_{x_{\mathrm{LUC}}(y')}^{x_{\mathrm{WA}}(y')} dx\, w^*_{\mathrm{LC}}, \quad \text{and} \tag{6c}$$

$$\mathcal{W}_b(y,t) \equiv \int_{y_s}^{y} dy' \int_{x_{\mathrm{LUC}}(y')}^{x_{\mathrm{WA}}(y')} dx\, w^*_b, \tag{6d}$$

where $w_b^* \equiv -\nabla \cdot \mathbf{V} = -\nabla \cdot (\mathbf{V}_{\rm LC} + \mathbf{V}_{\rm LUC})$ is the transport across the surface $z = -d_b$, $y_s = 34°$S, and the contour integration is taken along $x_{\rm LUC}(y)$. Integrating the equation of continuity yields

$$\mathcal{V}_{\rm LUC}(y,t) - \mathcal{V}_{\rm LUC}(y_s,t) = \mathcal{U}_{\rm LUC}(y,t) - \mathcal{W}_{\rm LUC}(y,t) + \mathcal{W}_b(y,t), \quad (6e)$$

indicating that the northward increase in the LUC transport is balanced by the cumulative inflow from the sidewall $x_{\rm LUC}(y)$ and the cumulative downwelling and upwelling across the top and bottom of the box, respectively.

Note that (4d) can be used as a definition of $\mathcal{W}_{\rm LC}$ instead of first calculating w^* from the equation of continuity and then using (4c). Likewise, (6e) can be used as a definition of $\mathcal{W}_{\rm LUC}$, because we choose the bottom of the LUC to coincide with the depth of no divergence d_b so that $\mathcal{W}_b$ identically vanishes. In this study, however, we calculate the transports $w_{\rm LC}^*$ and $w_{\rm b}^*$ first because we have to calculate the pointwise divergence of horizontal velocity for the ZD method anyway [see (2)] and because that method can be extended to the volume budget of a flow field where $\mathcal{W}_b \neq 0$. We design the discrete version of the equation of continuity and that of the contour integrals (4b) and (6b) in such a way that the volume balances (4d) and (6e) exactly hold.

3. Results

In this section, we first describe the LC, LUC, and SIO zonal flows determined from CARS. We conclude by reporting volume budgets that demonstrate the linkages among these currents.

a. *Leeuwin Current*

1) HORIZONTAL STRUCTURE

Figure 3 illustrates the horizontal structure of the near-surface, annual-mean flow field offshore from WA, plotting depth integrals of $\mathbf{v}_g'$ from $d_{\rm LC}$ to the surface (arrows) and indicating their meridional components (shading). There are two sources of water for the LC. One source is a southward inflow from the tropics (visible between 113° and 114°E along the equatorward edge of the plot), which has contributions from the eastward Eastern Gyral Current near 15°–20°S (Meyers et al. 1995; Domingues et al. 2007; Menezes et al. 2013) and from the shallow flows on the North West Shelf near 20°–22°S (Wijffels et al. 2008). The other is from eastward-flowing interior currents (jets) offshore from WA (Domingues et al. 2007; Divakaran and Brassington 2011; Menezes et al. 2014). The strongest of the jets is centered near 24°S, and it clearly drives the LC acceleration there. Farther south, weaker eastward (westward) interior currents are associated with accelerations (decelerations) of the LC. These narrow, eastward flows appear to correspond to Menezes et al.'s (2014) "central" and "southern" South Indian Countercurrents. Additionally, eddylike, small-scale features are ubiquitous. Some of them may be due to inadequate spatial and temporal coverage of observations that went into CARS, but the long-term mean OFAM3 velocity field shows similar features (see the appendix), suggesting that some, if not all, of them are real semipermanent features. Surprising to us, the LC transport does not increase to the south despite the predominance of eastward flow into the LC, a property that results from strong and fairly uniform downwelling out of the LC layer (see the discussions of Figs. 5 and 11a below).

2) VERTICAL STRUCTURE

Figure 4 plots zonal sections of annual-mean v_g' determined from CARS at six latitudes along the WA coastline. The LC is clearly defined in all the sections as the region of negative flow (blue shading) adjacent to the continental slope above 200 m. Very near the coast where $D < 100$ m, the equatorward-flowing Ningaloo (22°–24°S) and Capes (29°–34°S) Currents (Fig. 3), which are driven by the southerly alongshore winds (Cresswell et al. 1989; Pearce and Pattiaratchi 1999; Woo et al. 2006; Furue et al. 2013), are also visible, although their accuracy is dubious. For one thing, error of the geostrophic calculation is not small in shallow waters (Fig. 1); for another, these equatorward currents, though weaker, exist even in winter in our velocity field (not shown), whereas observations indicate that they exist only in summer, when the southerly winds are strongest (e.g., Woo et al. 2006).

The section at 22°S illustrates the structure of the LC that originates in the tropics. Along the entire coast, although the width and strength of the LC vary, its vertical extent does not, largely staying at 200 m, contrary to Furue et al.'s (2013) and Benthuysen et al.'s (2014) theoretical prediction. The bottom of the LC in OFAM3 also largely stays at 200 m along the entire coast (not shown).

3) SEASONAL AND ALONGSHORE VARIABILITY

Figure 5 plots LC transports $\mathcal{V}_{\rm LC}$ versus latitude for the annual mean (black solid) as well as during May (gray solid) and October (gray dashed), the months when the meridionally averaged LC transport has its maximum (1.6 Sv) and minimum values (0.6 Sv), respectively (discussed next). A striking property of the curves is the presence of large-amplitude, smaller-scale

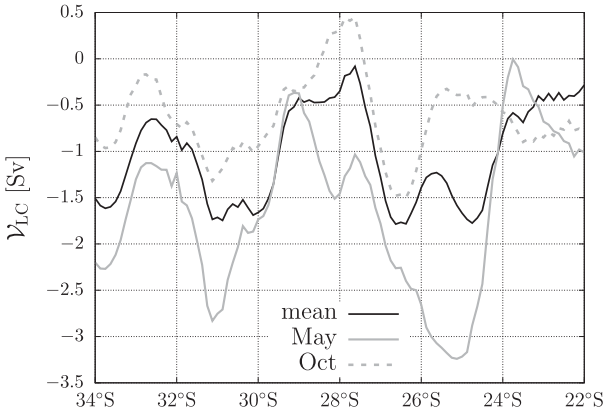

FIG. 5. LC geostrophic transports vs latitude based on CARS with the ZD method, illustrating the alongshore variation of the LC throughout the annual cycle.

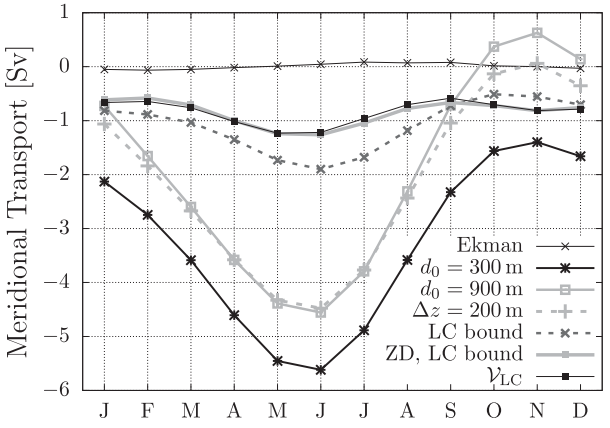

FIG. 6. LC geostrophic transports vs time at 32°S, showing the meridional geostrophic velocity using the HH method integrated from 110°E to the coast of Australia and from the sea surface to 300 m with $d_0 = 300$ m (thick, black, solid) and $d_0 = 900$ m (thin, light gray, solid); $d_0 = 900$ m, but the integration is limited to 200-m depth (light gray, dashed); same but the lower bound of the zonal integration is from $x_{LC}(32°S) = 114.5°E$ (dark gray, dashed); same but using the ZD method (thick, light gray, solid); and the same but the Ekman transport is added (thin, black, solid with filled squares). Finally, the thin, black, solid curve with crosses shows the Ekman transport integrated from $x_{LC}(32°S)$ to the coast of Australia.

(2°–4°) variations. They are caused by interactions of adjacent eddies and jets with the LC, as demonstrated by similar variations occurring in the SIO onshore flow (Fig. 3 and Figs. 9 and 11a below.) The LC reversal during October from 27° to 29°S and the very strong LC during May from 24.5° to 26.5°S result from the interaction of particularly strong eddies with the LC. Another noteworthy property of the curves is the lack of a distinct north-to-south increase in $|\mathcal{V}_{LC}|$. This lack contrasts with the LC theories mentioned in the introduction [section 1a(1)], in which most (all) of the SIO onshore flow turns southward to join the LC; it indicates that there must be a considerable loss of LC water to downwelling (section 3d).

Figure 10 (below) illustrates the annual cycle of the meridionally averaged LC transport (solid curve with symbols). It shows a clear, annual period, with the strongest (weakest) LC during May (October). The LC also tends to be wider when it is stronger (not shown), consistent with Huang and Feng's (2015) finding from satellite sea surface temperature (SST) data that the high SST region associated with the LC is wider when the LC is stronger. The vertical extent of the LC does not vary much in time and does not seem to have a systematic annual cycle (not shown).

4) COMPARISON WITH FENG ET AL. (2003)

The LC transport values in Fig. 5 are weaker than those reported in other studies. For example, Feng et al. (2003) estimated considerably larger LC transports at 32°S than we find in CARS, the discrepancy varying from a minimum of 1.5 Sv in February to 3.5 Sv in June. Their transport calculation differs from ours in that they used a reference level of 300 m and an empirical temperature–salinity relationship to compute geostrophic velocities from temperature observations and in that they defined the offshore boundary of the LC to be 110°E, much farther offshore than the core of the current.

To investigate the impact of these specifications, we calculate various meridional transports across 32°S (Fig. 6). The thick, black, solid curve shows meridional geostrophic velocity using the HH method with $d_0 = 300$ m integrated from 110°E to the coast of Australia and from 300 m to the sea surface. As expected, this curve shows similar magnitudes (1.5–5.5 Sv) to Feng et al.'s. When the reference level is increased to 900 m (thick, gray, solid), the transport is reduced by 1–2 Sv and is even reversed during October–December. The maximum transport (negative peak) is still as large as 4.5 Sv. The transports change little when the extent of vertical integration is reduced to $d_1 = 200$ m (thick, light gray, dashed) except that the reversed transports during October–December almost vanish. When the zonal extent of the integration is reduced to $x_{LC}(32°S) = 114.5°E$ (dark gray, dashed), the transports dramatically decrease during February–August and increase somewhat during October–December. Finally, when the geostrophic velocity field is adjusted with the ZD method (thick, gray, sold), the transports change by ~0.5 Sv. The difference between the HH and ZD methods are largest near this latitude (not shown). The impact of the Ekman transport (thin, solid, black with crosses) is very minor (thin, solid with filled squares).

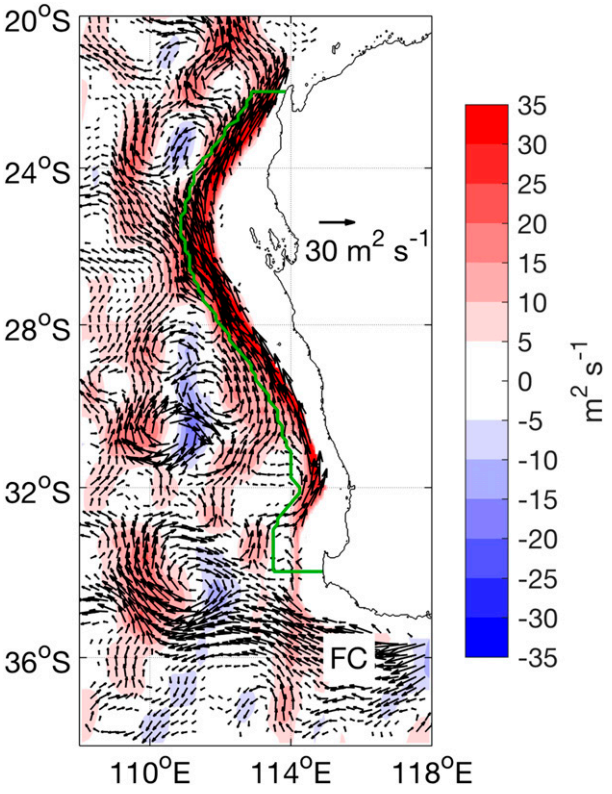

FIG. 7. As in Fig. 3, but integrated from $z = -900$ to -200 m. The green line is $x_{\mathrm{LUC}}(y)$ and the northern and southern edges of the LUC box (section 2d). The text FC indicates the Flinders Current.

The main reason for the discrepancy between Feng et al.'s transports and ours is, therefore, the zonal extent of integration. (The empirical temperature–salinity relationship is not likely to be a major factor because our geostrophic calculation with $d_0 = 300$ m and $x_{\mathrm{LC}} = 110°$E gives sufficiently similar values to Feng et al.'s.) Figures 3 and 4 indicate that our definition $x_{\mathrm{LC}}(y)$ of the offshore edge includes only the part of the poleward flow that is trapped on the continental slope. A wider integration range inevitably includes recirculations and eddies, and the resulting meridional transport values vary widely from latitude to latitude and from month to month (not shown).

b. *Leeuwin Undercurrent*

1) HORIZONTAL STRUCTURE

Figure 7 plots the depth integral of annual-mean $\mathbf{v}'_g$ from d_b to d_{LC}. The equatorward-flowing LUC begins at Cape Leeuwin (34°S), where it is fed by a northward bend of a small fraction of the Flinders Current and it extends to the Northwest Cape (22°S). It strengthens from 34°S (0.2 Sv) to 27.5°S (3.2 Sv), where it has a maximum throughout the year (Fig. 8). The LUC also broadens northward (see also Fig. 4). This feature is also found in OFAM3 (Fig. A1 below) and may be due to the broadening of the slope (slope being less steep; see Fig. 4). As for the LC, smaller-scale alongshore variations of the LUC in Fig. 7 appear to be linked with eddies and meanders that merge with the LUC. Meuleners et al. (2007) noted this interaction poleward of 30°S.

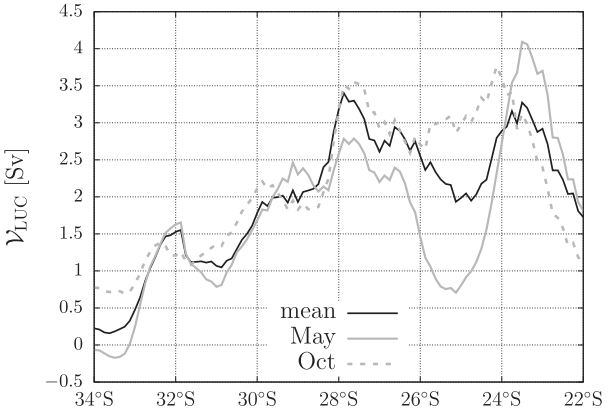

FIG. 8. As in Fig. 5, but for the LUC.

2) VERTICAL STRUCTURE

As evident in Fig. 4, the vertical structure of the LUC changes markedly along the coast, its core tending to shoal to the north: the core depth lies at 450 m at 34°S and shallows to 370 m at 26°S. Additionally, its upper boundary rises northward, in many of the sections lying along the outer flank of the LC and even appearing to reach the surface at 28°S. Much (if not all) of the shallowing must result from downwelling across the bottom of the LC (Fig. 11b below), which adds less-dense water to the top of the LUC. The apparent surfacing at 28°S, however, is caused by the superposition of a near-surface anticlockwise eddy (28°S, 112°E; Fig. 3) and so is not indicative of LUC shallowing at this location. At other latitudes (near 26° and 30°S), the apparent surface extensions of the LUC (Fig. 4) are in fact isolated regions of equatorward flows just offshore from the LCS (Fig. 3). At some latitudes, such as 30°S, these near-surface flows extend to the depth range of the LUC (Fig. 4), but, with our definitions of current boundaries (section 2d), contributions from these offshore regions are not included in the LUC.

3) SEASONAL AND ALONGSHORE VARIABILITY

Figure 8 plots LUC transports $\mathcal{V}_{\mathrm{LUC}}$ versus latitude for the annual mean (black, solid) as well as during May (gray, solid) and October (gray, dashed), the months when the meridionally averaged LUC transport has its minimum (1.7 Sv) and maximum values (2.2 Sv), respectively (not shown). In contrast to the LC, all three

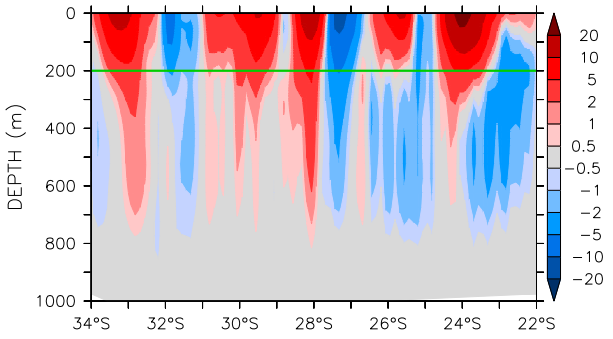

FIG. 9. The component of the annual-mean, geostrophic velocity $\mathbf{v}_g'$ (cm s^{-1}) normal to the outer edge of the LUC, $x_{\mathrm{LUC}}(y)$. The horizontal green line is the bottom of the LC box, d_{LC} (section 2d). To emphasize weak flow, the contour intervals are quasi logarithmic. The small-scale noise (~0.5°) is because the lateral boundaries of the LUC box are not smooth, as they follow the CARS grid. See the green curve in Fig. 7. To alleviate the problem, a 1–2–1 meridional smoothing has been applied to the normal velocity field.

curves have a prominent large-scale structure, with $\mathcal{V}_{\mathrm{LUC}}$ increasing from 34° to 28°S and decreasing rapidly north of 24.5°S. Between 28° and 24.5°S, $\mathcal{V}_{\mathrm{LUC}}(y)$ is relatively constant in October and has a relative minimum in May, the latter because of an offshore detour of the LUC during May–September (not shown). There is no clear annual cycle in other latitude ranges.

The LUC is weak at 34°S: only a tiny fraction of the Flinders Current bends equatorward at Cape Leeuwin (34°S, 114°E) to form the LUC; the rest continues westward, some fraction of the latter turning back to join the LUC equatorward of 33°S (Fig. 7; Duran 2015). This loop appears to form around and above the Naturaliste Plateau (35°–33°S, 110°–113°E), visual correlation of the transport-velocity vectors with the bottom topography being very high (not shown), even though the shallowest point of the plateau is still much deeper than the bottom of the LUC. Meuleners et al. (2007) reported a similar loop in their ocean general circulation model, but their Flinders Current turns back onshore just poleward of the peak of the plateau (34°S); the reason for this discrepancy is not known.

c. *SIO zonal flows*

To illustrate the vertical structure of the interaction of the SIO zonal flows with the LC and LUC, Fig. 9 shows the component of the annual-mean, geostrophic velocity $\mathbf{v}_g'$ normal to $x_{\mathrm{LUC}}(y)$, the outer boundary of the LUC (section 2d). The LUC outer boundary is chosen over the LC boundary because the normal velocity into or out of the LUC box is better represented along $x_{\mathrm{LUC}}(y)$, whereas the upper-layer normal flows are not much different between $x_{\mathrm{LUC}}(y)$ and $x_{\mathrm{LC}}(y)$ (not shown). The near-surface normal flow is primarily surface trapped ($z > -200$ m), its depth range consistent with that of the LC (Fig. 4), is dominated by inflows (eastward flows), and is split into a set of 6–7 eastward jets with maximum surface velocities of ~10 cm s^{-1}.

The jets near 24°S and 28°–30°S are consistent with the previously identified ones [Menezes et al. 2014; section 3a(1); Fig. 3]. Below the near-surface layer, the subsurface flows tend to be directed onshore (eastward) south of 28°S and offshore (westward) north of it and, like the near-surface flow field, are divided into a series of jets. The inflows south of 28°S are consistent with those in the horizontal map (Fig. 7) discussed above.

Domingues et al. (2007) was based on analysis of the Parallel Ocean Program model, run 11B eddy-permitting OGCM (POP11B; Maltrud et al. 1998). Further analysis was presented in the Ph.D. thesis of Domingues (2006), including a 5-yr mean zonal velocity averaged from the outer edge of the LC (Domingues's definition) to the coast of Australia (her Fig. 5.2). Like our zonal velocity (Fig. 9), the velocity structure of Domingues (2006) changes around 200-m depth, with eastward flows dominating above 200 m and several zonal jets superimposed. Her lower-layer zonal velocity is, however, dominated by westward flows throughout the latitude range 34°–22°S, whereas CARS is dominated by inflows south of 28°S (Fig. 9). In OFAM3 (Figs. A1 and A2 below), there is no net inflow south of 28°S in the lower layer either. This difference between CARS and the two numerical models could be due to the lack of the retroflection of the Flinders Current in the models for an unknown reason.

Note that some of the strong westward jets are located beneath regions of weak eastward flow and vice versa, suggesting that the surface and subsurface jets are formed by the same process, one that occurs relatively uniformly over the depth range from 900 m to the ocean surface. [A meridionally high-pass filtered version of this plot (not shown) reveals a series of vertically coherent zonal jets of alternating signs. To see its vertical structure more clearly, we examined the CARS geostrophic flow with $d_0 = 2000$ m along 111°E (not shown), finding clear zonal jets of alternating signs extending well below 1000 m south of 28°S (those to the north were less coherent). Similar features have been discussed in the literature (e.g., Divakaran and Brassington 2011; Taguchi et al. 2012; Qiu et al. 2013; and references therein).

To measure the seasonal impact of the SIO flows, Fig. 10 plots the net zonal transport into the LC and LUC from the SIO versus time, that is, $\mathcal{U}_{\mathrm{LC}}(y_{\mathrm{s}})$ and $\mathcal{U}_{\mathrm{LUC}}(y_{\mathrm{n}})$, respectively. In addition, it plots the meridional integral of the surface Ekman transport across $x_{\mathrm{LC}}(y)$,

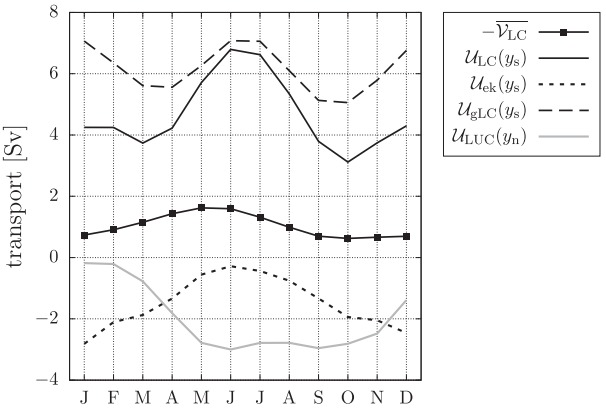

FIG. 10. Transport curves integrated or averaged along the WA coast vs time, showing meridional transport $-\mathcal{V}_{LC}$ averaged over 34°–22°S; $\mathcal{U}_{LC}(y_s)$ and $\mathcal{U}_{LUC}(y_n)$, the total zonal transports into or out of the LC and LUC, respectively. In addition, the figure plots the meridional integral of the surface Ekman transport across $x_{LC}(y)$, $\mathcal{U}_{ek} = \int_{y_s}^{y_n} \mathbf{n} \cdot (-\mathbf{k} \times \boldsymbol{\tau}/\rho_o f)\, dy$ (dotted), as well as the difference $\mathcal{U}_{gLC} \equiv \mathcal{U}_{LC} - \mathcal{U}_{ek}$ (dashed).

$\mathcal{U}_{ek} = \int_{y_s}^{y_n} \mathbf{n} \cdot (-\mathbf{k} \times \boldsymbol{\tau}/\rho_o f)\, dy$ (dotted), as well as the difference $\mathcal{U}_{gLC} = \mathcal{U}_{LC} - \mathcal{U}_{ek}$ (dashed)—the latter presumably density driven. A comparison of the curves shows that the seasonal variability of $\mathcal{U}_{LC}$ is a superposition of the annual variability (~2 Sv) of $\mathcal{U}_{ek}$ and the semiannual variability (~2 Sv) of $\mathcal{U}_{gLC}$. Similarly to the zonal inflow into the LC box (solid black), the zonal outflow from the LUC box (solid gray) reaches a maximum in June, but its semiannual component seems weaker.

Although the amplitudes are very different [section 3a(4)], the annual cycle of the mean LC transport $\overline{\mathcal{V}_{LC}}$ from CARS is consistent with past results, where the maximum and minimum transports occur around June and October–January, respectively (e.g., Feng et al. 2003). It is also similar to the annual cycle of the total lateral inflow $\mathcal{U}_{LC}(y_s)$ except that $\overline{\mathcal{V}}$ leads by 1 month and that the latter's semiannual component is less prominent. Given the net downwelling from the LC and LUC (see the next section), the significance of these similarities and differences is not clear.

d. Volume budgets

To illustrate interactions between the LC, LUC, and SIO currents, Fig. 11 plots annual-mean transports across the faces of the LC and LUC boxes defined in section 2d. Transport $\mathcal{U}_{LC}$ has a net inflow to the LCS from the SIO interspersed with regions of offshore flow, where $\partial\mathcal{U}_{LC}/\partial y > 0$. These small-scale variations in $\mathcal{U}_{LC}$ are reflected in $|\mathcal{V}_{LC}|$, with onshore flow ($\partial\mathcal{U}_{LC}/\partial y < 0$) associated with the poleward acceleration of the LC ($\partial|\mathcal{V}_{LC}|/\partial y < 0$) and offshore flow with the poleward

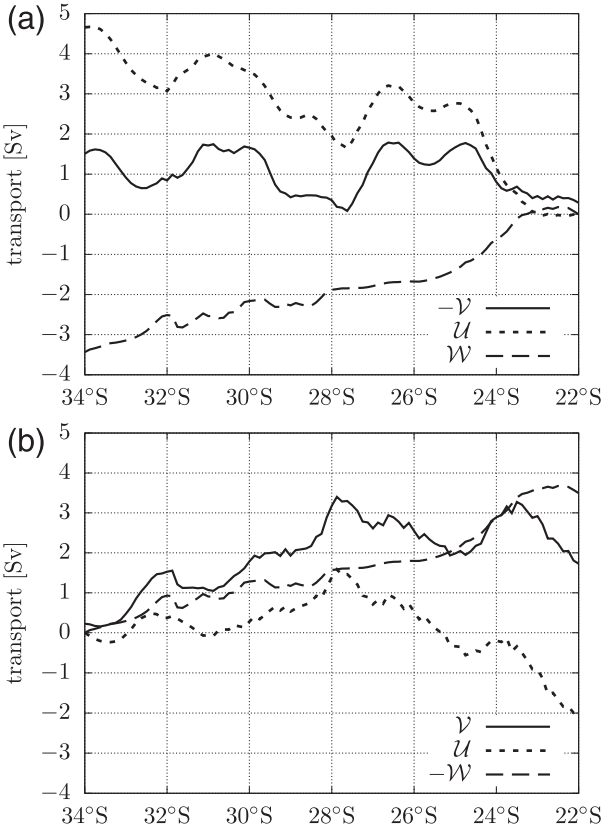

FIG. 11. Annual-mean transport curves vs latitude for (a) the LC box showing $-\mathcal{V}_{LC}$ (solid), $\mathcal{U}_{LC}$ (dotted), and $\mathcal{W}_{LC}$ (dashed), and (b) the LUC box showing $\mathcal{V}_{LUC}$ (solid), $\mathcal{U}_{LUC}$ (dotted), and $-\mathcal{W}_{LUC}$ (dashed); $\mathcal{W}_b$ is not plotted because the ZD correction makes it identically zero. See section 2d for the definitions of the boxes and these variables.

deceleration, a consequence of the eddy-like circulation interacting with the LC (Fig. 3). Remarkably, $|\mathcal{V}_{LC}(y)|$ does not steadily increase in response to the net onshore flow $\mathcal{U}_{LC}$, a consequence of water sinking out of the LC due to $\mathcal{W}_{LC}(y)$. Further, the sinking occurs fairly uniformly ($\partial\mathcal{W}_{LC}/\partial y$ is roughly constant), so that most of the small-scale variations in $\mathcal{U}_{LC}(y)$ are absorbed by $\mathcal{V}_{LC}(y)$. This striking difference between the horizontal and vertical transports points toward the dynamics of the downwelling being independent of the eddylike structures. On average, the LC accelerates from 0.3 Sv at y_n to 1.5 Sv at y_s, the acceleration a result of the net inflow of 4.7 Sv [$\mathcal{U}_{LC}(y_s)$] minus the net downwelling of 3.4 Sv [$|\mathcal{W}_{LC}(y_s)|$; to close the budget for the LC box, this number has to be 3.5 Sv, a discrepancy due to rounding]. The eastward inflow from the SIO thus contributes more to the LC transport than the direct poleward inflow from the tropics (see also Fig. 3), an indication of the importance of the interior forcing. We have carried out the same analysis on the OFAM3 velocity field (see the

appendix) and on the geostrophic calculation based on the OFAM3 *T*–*S* field (not shown), finding that all the above properties qualitatively hold for OFAM3.

Figure 11b shows curves similar to those in Fig. 11a, except evaluated for the LUC box. Even though the upper surface of the LUC box does not exactly coincide with the lower surface of the LC box (Fig. 4), virtually all downwelling through the bottom of the LC box enters the LUC box [mathematically, $\mathcal{W}_{\rm LUC}(y) \simeq \mathcal{W}_{\rm LC}(y_{\rm s}) - \mathcal{W}_{\rm LC}(y)$], the difference being negligible in some months and at most ~0.1 Sv in others (not shown); this is because most downwelling occurs very near the coast (not shown). Note that the transport through the bottom of the LUC box (6d), which vanishes owing to the ZD correction, is not plotted.

The LUC at 34°S, representing the part of the Flinders Current bending northward at Cape Leeuwin (Fig. 7), is very weak (0.2 Sv; Fig. 11b). As the LUC flows northward, $\mathcal{V}_{\rm LUC}(y)$ strengthens in response to $|\mathcal{W}_{\rm LUC}|$ and to a lesser extent to $\mathcal{U}_{\rm LUC}$, the latter including the retroflection of the Flinders Current (Fig. 7), and reaches a peak value at 28°S. Farther north, water loss due to $\mathcal{U}_{\rm LUC}$ overwhelms $|\mathcal{W}_{\rm LUC}|$, and $\mathcal{V}_{\rm LUC}(y)$ weakens (see also Fig. 7). As for the LC, smaller-scale changes in $\mathcal{V}_{\rm LUC}(y)$ are linked to those of $\mathcal{U}_{\rm LUC}$. The net increase in the LUC transport from $y_{\rm s}$ to $y_{\rm n}$ is 1.5 Sv, a result of 3.5 Sv of downwelling $|\mathcal{W}(y_{\rm n})|$, minus 2 Sv of net offshore flow $|\mathcal{U}(y_{\rm n})|$. The corresponding results from OFAM3 are qualitatively similar, except that the LUC is not weak at 34°S nor does it systematically accelerate equatorward (see the appendix), the difference likely due to the lack of the Flinders Current retroflection in the model (see the appendix).

4. Summary and discussion

In this study, we use a high-resolution (1/8°), hydrographic dataset (CARS) to build a more complete picture of the mean and seasonal cycle of the Leeuwin Current System (LCS). Based on geostrophic currents obtained from CARS, we describe the spatial structure and annual variability of the Leeuwin Current (LC), Leeuwin Undercurrent (LUC), and south Indian Ocean (SIO) zonal currents, estimate their transports, and identify linkages among them. We use two methods to determine geostrophic velocities. The first (and traditional) one adopts a level of no motion d_0 offshore and sets the alongshore velocity to zero on the shelf/slope (HH). A limitation of this approach, however, is that it allows flow across the bottom of the shelf/slope and therefore mass is not conserved. The second method, the one we use for most of our analyses, assumes that vertical velocity vanishes offshore at d_0 and explicitly requires that there is no across-bottom flow nearshore [the zero divergence (ZD) method]. We checked the validity of both methods by applying them to the OFAM3 solution: They both produce reasonable alongshore flow fields provided that $d_0 \sim 1000$ m (Fig. 1). For smaller d_0, they lose accuracy since the reference-level velocity contains the equatorward-flowing LUC (Fig. 2), and for larger d_0, the upper circulation starts to disintegrate because of (spurious) vertical shear in the model outputs near the bottom.

In CARS, the LC is located just off the WA shelf and is almost always directed poleward (Figs. 3, 4). Its strength, however, varies considerably along the coast due to jets and eddies; as a result, the LC can be quite weak or even reverse at some times and locations (Fig. 5).

The LC has a prominent annual cycle, attaining maximum values almost everywhere along the coast during May–June (Fig. 5). McCreary et al. (1986) argue that this seasonal variability is driven by the alongshore winds, which are weakest during May; the weaker southerly winds at that time decrease the offshore Ekman transport, thereby intensifying the net onshore flow that merges with the LC (section 3c). Ridgway and Godfrey (2015), on the other hand, argue that the seasonal variability of the LC is largely due to that of sea levels on the northern and northwestern shelf regions driven by winds and surface heat flux.

Our data are consistent with the former mechanism in that the seasonality of the onshore flow ($\mathcal{U}_{\rm LC}$) is dominated by that of the Ekman drift and is similar to that of the LC strength (Fig. 10). Since a large fraction of $\mathcal{U}_{\rm LC}$ is lost to downwelling, however, the impact of $\mathcal{U}_{\rm LC}$ on the meridional transport of the LC is uncertain, unless the mechanism that drives $\mathcal{W}_{\rm LC}$ is clear. The latter mechanism, on the other hand, should manifest itself as a seasonality in the inflow across the northern edge of the LC box [$\mathcal{V}_{\rm LC}(y_{\rm n})$]. Unfortunately, we found that the seasonal cycle of $\mathcal{V}_{\rm LC}(y_{\rm n})$ is strongly contaminated by that of local eddylike recirculations (not shown), obscuring the role of signals from the north.

Interestingly, there is a distinct semiannual variability in the geostrophic component of the onshore flow ($\mathcal{U}_{g\rm LC}$; Fig. 10). This variability could be related to the monsoon, but details are not known.

Throughout the year, our LC transport values tend to be smaller than estimates by other researchers. Most of these studies are based on hydrographical snapshots or current meter moorings (e.g., Smith et al. 1991), the former including more energetic eddylike features and the latter not having sufficient horizontal resolution to separate the LC from offshore flows. We investigated the cause of the difference between our estimate of LC

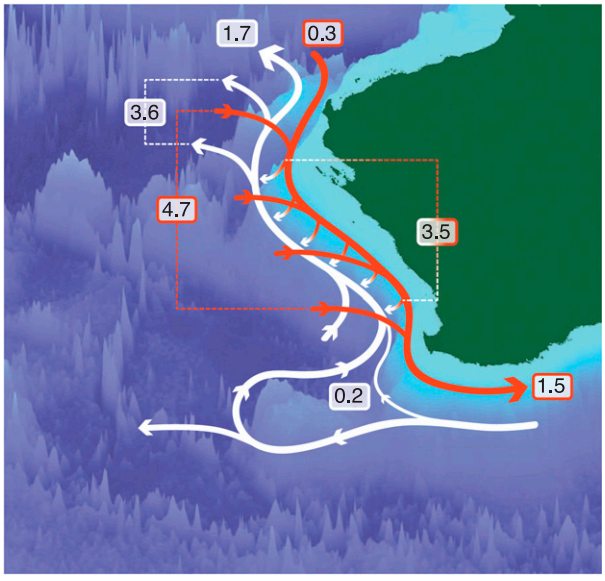

FIG. 12. A schematic summary of the LCS flow based on the geostrophic calculation on CARS Aus8. The red and white arrows represent upper- and lower-layer flows, respectively. The numbers are annual-mean volume fluxes in Sverdrups. See section 4 for details. [The downwelling from the bottom of the LC box is quoted as 3.4 Sv and that through the upper face of the LUC box as 3.5 Sv in the text. This slight difference is because the upper surface of the LUC box does not exactly coincide with the lower surface of the LC box (Fig. 4), and the slight difference in transport is exaggerated by rounding.]

transport at 32°S and Feng et al.'s (2003), both of which are based on historical hydrographical data (Fig. 6). We found that the transport estimate is sensitive to the choice of level of no motion; choosing a level within the equatorward LUC (300 m as in Feng et al.) artificially increases the LC poleward transport. However, the strongest influence on the LC transport comes from the choice of the offshore limit of integration. Our integration limit varies with latitude to include only the poleward flow that is trapped to the coast. Integrating farther offshore (110°E in Feng et al.) artificially increases or decreases the LC poleward flow by including offshore meridional flows.

It is not known whether there is a mean poleward flow offshore of the core of the LC apart from the semipermanent eddies and meanders discussed in section 3a(1). M. Feng (2016, personal communication) and one anonymous reviewer suggested that the LC may have an offshore branch. Our view is that the LC is a poleward flow that is trapped to the continental slope/shelf and a poleward flow away from the slope is a dynamically different phenomenon, like the one off the coast of California (the Davidson Current), which is likely a Sverdrup flow driven by cyclonic wind curl (McCreary et al. 1987).

Figure 12 provides a schematic summary of the mean LCS flow. The LC is supplied by water from the tropics (0.3 Sv crosses 22°S in the annual mean) and by shallow ($z > -200$ m) eastward flows from the SIO (a net of 4.7 Sv integrated between 22° and 32°S), and it loses water through downwelling across its bottom (3.4 Sv; Fig. 11a). The shallow eastward flows thus contribute more to the LC transport than the poleward inflow at 22°S, an indication of the importance of the interior SIO forcing. Remarkably, the downwelling transport $|\mathcal{W}|$ is so strong that, despite the SIO inflow, the LC transport does not strengthen much as the current moves poleward. Additionally, $\mathcal{W}$ varies relatively linearly along the coast with only weak, smaller-scale variability, suggesting that the downwelling is not primarily caused or affected by eddy–mean flow interactions.

The LUC is present from 200 to 800 m along the WA continental slope, extending from Cape Leeuwin to the North West Shelf (Figs. 4, 7), and, like the LC, it exhibits prominent smaller-scale variations due to eddies and jets. These small-scale features tend to be vertically coherent to a depth of ~1000 m. As such, they are reminiscent of so-called striations (e.g., Nakano and Hasumi 2005; Maximenko et al. 2008; Taguchi et al. 2012), although the local velocity tends to change sign vertically because of the superimposed large-scale baroclinic flow (Fig. 9 and its discussion in section 3c). The annual cycle of the LUC is negatively correlated with that of the LC, its meridionally averaged transport having its minimum during May and its maximum during October.

At Cape Leeuwin, the LUC is supplied by water from the Flinders Current south of Australia (0.2 Sv crosses 34°S in Fig. 11b; Fig. 12). As it flows north, it is strengthened by downwelling from the LC and onshore flow from the SIO, the latter including an offshore retroflection of the Flinders Current (Fig. 12). The LUC then attains its maximum transport (3.4 Sv) at 28°S; farther equatorward, it starts to lose water by outflow into subsurface flow in the SIO. On average, the LUC accelerates by 1.5 Sv from 34° to 22°S, a result of a net downwelling of 3.5 Sv minus a net offshore flow of 2 Sv (Fig. 12).

Despite considerable effort (section 1), basic dynamics of the LCS remain unclear, particularly concerning the LUC. The McCreary et al. (1986) solution is appealing because it captures most of the LCS features in CARS within a simple theoretical framework, but given its deficiencies [section 1a(2)], it is not clear how accurately the model represents basic LCS dynamics.

Studies have indicated that the near-surface eastward flow is driven by the meridional density gradient [section 1a(3)]. In contrast, the forcing of the subsurface

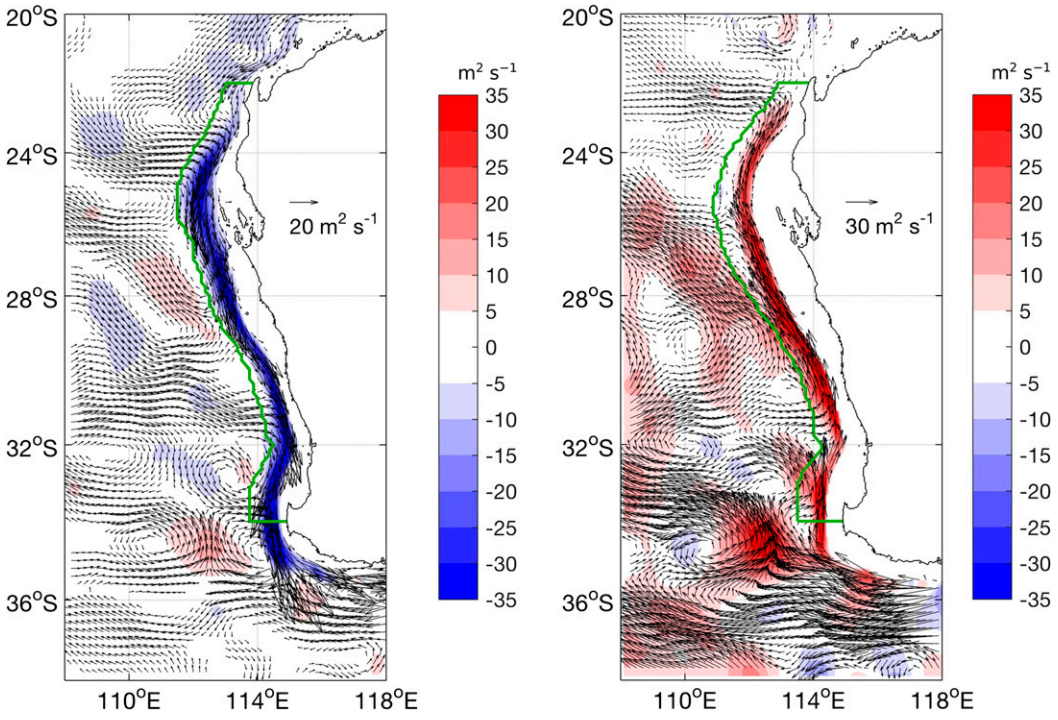

FIG. A1. Maps of vertically integrated annual-mean velocities (arrows), with its meridional component $\int v\,dz$ shaded ($m^2\,s^{-1}$). The integration is over the (left) LC ($-200 < z < 0$ m) or (right) LUC ($-900 < z < -200$ m) depth range. The green lines are $x_{LC}(y)$ or $x_{LUC}(y)$ and the northern and southern edges of the LC or LUC box (section 2d).

westward outflow from the LUC is less clear. In the McCreary et al. (1986) model, it results from the propagation of weakly damped Rossby waves from the eastern boundary. It may also be part of the Sverdrup gyre in the south Indian Ocean, at least sufficiently far offshore.

In conclusion, CARS provides a comprehensive, observational picture of the LCS flow field, and its properties point toward strong dynamical linkages among all its currents; near-surface eastward flow from the SIO merges with the LC, downwells into the LUC, and eventually bends offshore to join subsurface westward flow in the SIO. Of particular importance, the CARS data point to downwelling from the LC as being a key process; it provides a sink of water for the LC that prevents it from accelerating poleward and conversely is a source for the LUC that allows it to strengthen equatorward.

The CARS results highlight a number of dynamical questions that are not answered by existing theories and models. They include the following: 1) Just what processes cause the large and uniform $\mathcal{W}$ along the LC, and does it occur diapycnally or isopycnally? 2) How does downwelled LC water actually merge with the LUC? Is this the water that appears on the outer flanks of the LC (Fig. 4)? 3) What processes cause the subsurface westward flow in the SIO? Does offshore propagation of Rossby waves lead to westward flow even when there is a shelf? 4) What are the basic dynamics of the LUC? We expect our CARS results provide guidelines for answering these questions, thereby leading to the development of more complete theories.

Acknowledgments. This study was supported by the Australian Research Council Discovery Projects (DP 130102088) and by the National Science Foundation through Grant OCE-0961716. RF was partially supported by the Japan Society for the Promotion of Science through KAKENHI 16K05562. We thank Jeff Dunn for updating the CARS Aus8 dataset (http://www.marine.csiro.au/atlas/) for this study. Thanks are extended to Catia Domingues, Earl Duran, Ming Feng, Viviane Menezes, Gary Meyers, Ken Ridgway, and Fabian Schloesser (alphabetical order) for helpful discussion. Comments from anonymous reviewers helped significantly improve and clarify this manuscript. We also acknowledge use of the Ferret program for analysis and graphics in this paper. Ferret is a product of NOAA's Pacific Marine Environmental Laboratory. (Information is available at http://ferret.pmel.noaa.gov/Ferret/.)

APPENDIX

Results from OFAM3 and OFES

This appendix briefly compares the horizontal structures and volume budgets of the LC ($z > -200$ m) and LUC ($-900 < z < -200$ m) layers from the long-term mean OFAM3 absolute velocity to those from the CARS geostrophic velocity (Figs. 3, 7, 11).

Figure A1 shows the maps of the OFAM3 velocity integrated over the LC (left) and LUC (right) depth ranges. It is noteworthy that even the average over 13 yr includes eddylike features similar to those in the CARS field (Figs. 3, 7), although their amplitudes and locations are different and smaller-scale features are less prominent in OFAM3 than in CARS.

Figure A2 shows the same budget curves as Fig. 11 but for the OFAM3 absolute velocity field, which indicates that most of our conclusions on the CARS volume budgets (Fig. 11) hold. Namely, there is a net zonal inflow ($\mathcal{U}$ in Fig. A2a) into the LC box, a large portion of it sinks ($\mathcal{W}$) into the LUC box, and as a result, the LC transport ($\mathcal{V}$) is not as much strengthened as the zonal inflow suggests; there are small-scale, zonal inflow and outflow, which are reflected in the strengthening and weakening of the LC transport but not in the downwelling; and, despite this downwelling ($\mathcal{W}$, Fig. A2b) into the LUC box, the LUC decelerates on average because of the net outflow ($\mathcal{U}$, Fig. A2b).

One difference is that the net zonal inflow and downwelling for the LC box are smaller in OFAM3 (~3.5 Sv, ~2 Sv; Fig. A2a) than in CARS (~4.5 Sv, ~3.5 Sv; Fig. 11a). Another difference is that the smaller-scale features in $\mathcal{U}$ and $\mathcal{V}$ are somewhat less prominent in OFAM3 than in CARS, although there are climatological months when the smaller-scale features are much more prominent (not shown). Finally, in the LUC depth range, zonal outflow ($d\mathcal{U}/dy < 0$) dominates throughout the latitude range in OFAM3 (Fig. A2b), whereas inflow dominates south of 28°S in CARS (Fig. 11b); a related difference is that the LUC already has a significant transport at the poleward edge of our LUC box (34°S) in OFAM3, whereas it is very weak there in CARS. These differences are consistent with the difference in the horizontal flow pattern (Fig. A1 vs Fig. 7): some part of the Flinders Current bends equatorward at Cape Leeuwin (34°S) and directly feeds into the LUC in OFAM3, whereas most of the Flinders Current flows past the Cape, and part of it retroflects to join the LUC farther north in CARS.

Finally, we have made plots (not shown) comparable to Figs. A1 and A2 from another 1/10° eddy-resolving OGCM called OFES (Masumoto et al. 2004; Sasaki et al. 2008). The version of OFES used here is described in Sasaki et al. (2008) and is run under daily mean forcings derived from the NCEP–NCAR reanalysis (Kalnay et al. 1996) from 1950 to 2015. All properties stated above about OFAM3 qualitatively apply to the OFES results. In particular, eddylike features are still present in this 66-yr mean field although they are weaker than in OFAM3, and their locations are not always the same. The mean LC and LUC transports and associated zonal and vertical volume fluxes are also somewhat weaker.

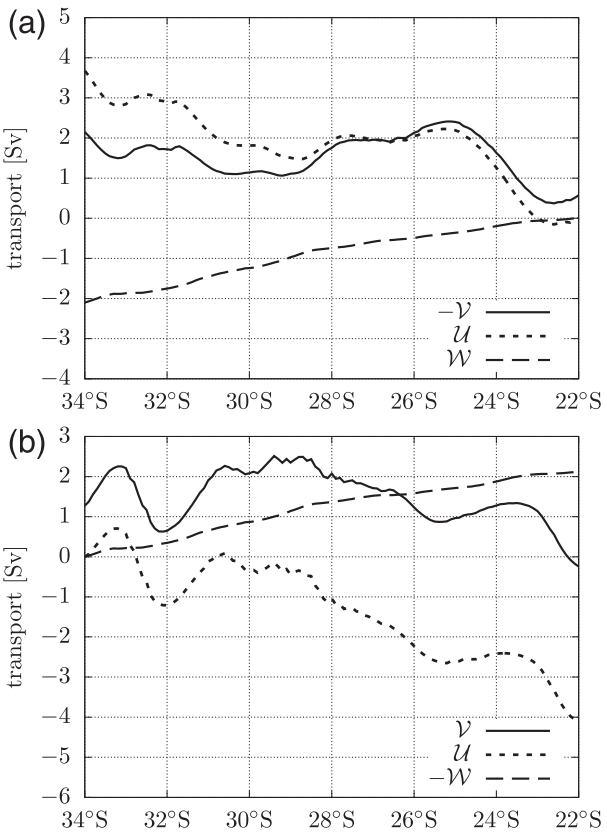

FIG. A2. The annual-mean volume flux curves based on the OFAM3 climatological absolute velocity field for (a) LC and (b) LUC. See caption to Fig. 11 for details. Note that the flux through the bottom of the LUC box is nonzero (because the velocity field is not from a ZD geostrophic calculation) but is not plotted.

REFERENCES

Akhir, M. F., and C. B. Pattiaratchi, 2006: Summer physical processes along the continental shelf and slope off southern Western Australia. *Proc. Sixth Int. Symp. on Stratified Flows*, Perth, Western Australia, G. N. Ivey, Ed., 239–244.

Andrews, J. C., 1983: Ring structure in the poleward boundary current off Western Australia in summer. *Aust. J. Mar. Freshwater Res.*, **34**, 547–561, doi:10.1071/MF9830547.

Benthuysen, J., R. Furue, J. P. McCreary, N. L. Bindoff, and H. E. Phillips, 2014: Dynamics of the Leeuwin Current: Part 2. The

role of mixing and advection in a buoyancy-driven eastern boundary current over a continental shelf. *Dyn. Atmos. Oceans*, **65**, 39–63, doi:10.1016/j.dynatmoce.2013.10.004.

Bingham, R. J., and C. W. Hughes, 2012: Local diagnostics to estimate density-induced sea level variations over topography and along coastlines. *J. Geophys. Res.*, **117**, C01013, doi:10.1029/2011JC007276.

Bye, J. A. T., 1972: Oceanic circulation south of Australia. *Antarctica Oceanology II: The Australian–New Zealand Sector*, Antarctic Research Series, Vol. 19, Amer. Geophys. Union, 95–100.

Church, J. A., G. R. Cresswell, and J. S. Godfrey, 1989: The Leeuwin Current. *Poleward Flows along Eastern Ocean Boundaries*, Coastal Estuarine Studies, Vol. 34, Amer. Geophys. Union, 230–254.

Cresswell, G. R., and T. J. Golding, 1980: Observations of a south-flowing current in the southeastern Indian Ocean. *Deep Sea Res.*, **27A**, 449–466, doi:10.1016/0198-0149(80)90055-2.

——, F. M. Boland, J. L. Peterson, and G. S. Wells, 1989: Continental shelf currents near the Abrolhos Islands, Western Australia. *Aust. J. Mar. Freshwater Res.*, **40**, 113–128, doi:10.1071/MF9890113.

Dee, D. P., and Coauthors, 2011: The ERA-Interim reanalysis: Configuration and performance of the data assimilation system. *Quart. J. Roy. Meteor. Soc.*, **137**, 553–597, doi:10.1002/qj.828.

Divakaran, P., and G. B. Brassington, 2011: Arterial ocean circulation of the southeast Indian Ocean. *Geophys. Res. Lett.*, **38**, L01802, doi:10.1029/2010GL045574.

Domingues, C. M., 2006: Kinematics and heat budget of the Leeuwin Current. Ph.D. thesis, Flinders University of South Australia, 156 pp.

——, M. E. Maltrud, S. E. Wijffels, J. A. Church, and M. Tomczak, 2007: Simulated Lagrangian pathways between the Leeuwin Current System and the upper-ocean circulation of the southeast Indian Ocean. *Deep-Sea Res. II*, **54**, 797–817, doi:10.1016/j.dsr2.2006.10.003.

Dunn, J. R., and K. R. Ridgway, 2002: Mapping ocean properties in regions of complex topography. *Deep-Sea Res. I*, **49**, 591–604, doi:10.1016/S0967-0637(01)00069-3.

Duran, E. R., 2015: An investigation of the Leeuwin Undercurrent source waters and pathways. Bachelor's of Marine Science with Honours thesis, Institute for Marine and Antarctic Studies, University of Tasmania, 112 pp.

Fang, F., and R. Morrow, 2003: Evolution, movement and decay of warm-core Leeuwin Current eddies. *Deep-Sea Res. II*, **50**, 2245–2261, doi:10.1016/S0967-0645(03)00055-9.

Feng, M., G. Meyers, A. Pearce, and S. Wijffels, 2003: Annual and interannual variations of the Leeuwin Current at 32°S. *J. Geophys. Res.*, **108**, 3355, doi:10.1029/2002JC001763.

——, S. Wijffels, S. Godfrey, and G. Meyers, 2005: Do eddies play a role in the momentum balance of the Leeuwin Current? *J. Phys. Oceanogr.*, **35**, 964–975, doi:10.1175/JPO2730.1.

Fratantoni, P. S., and R. S. Pickart, 2007: The western North Atlantic shelfbreak current system in summer. *J. Phys. Oceanogr.*, **37**, 2509–2533, doi:10.1175/JPO3123.1.

Frouin, R., A. F. G. Fiúza, I. Ambar, and T. J. Boyd, 1990: Observations of a poleward surface current off the coasts of Portugal and Spain during winter. *J. Geophys. Res.*, **95**, 679–691, doi:10.1029/JC095iC01p00679.

Furue, R., J. P. McCreary, J. Benthuysen, H. E. Phillips, and N. L. Bindoff, 2013: Dynamics of the Leeuwin Current: Part 1. Coastal flows in an inviscid, variable-density, layer model. *Dyn. Atmos. Oceans*, **63**, 24–59, doi:10.1016/j.dynatmoce.2013.03.003.

Godfrey, J. S., and K. R. Ridgway, 1985: The large-scale environment of the poleward-flowing Leeuwin Current, Western Australia: Longshore steric height gradients, wind stresses and geostrophic flow. *J. Phys. Oceanogr.*, **15**, 481–495, doi:10.1175/1520-0485(1985)015<0481:TLSEOT>2.0.CO;2.

——, and Coauthors, 1995: The role of the Indian Ocean in the global climate system: Recommendations regarding the global ocean observing system. Ocean Observing System Development Panel Background Rep. 6, 89 pp.

Griffies, S. M., 2009: Elements of MOM4p1. NOAA/Geophysical Fluid Dynamics Laboratory Ocean Group Tech. Rep. 6, 444 pp. [Available online at http://mdl-mom5.herokuapp.com/web/docs/project/MOM4p1_manual.pdf; http://www.gfdl.noaa.gov/fms/.]

Helland-Hansen, B., 1934: The Sognefjord section: Oceanographic observations in the northernmost part of the North Sea and the southern part of the Norwegian Sea. James Johnstone Memorial Volume, J. Johnstone and R. J. Daniel, Eds., 257–274.

Huang, Z., and M. Feng, 2015: Remotely sensed spatial and temporal variability of the Leeuwin Current using MODIS data. *Remote Sens. Environ.*, **166**, 214–232, doi:10.1016/j.rse.2015.05.028.

Kalnay, E., and Coauthors, 1996: The NCEP/NCAR 40-Year Reanalysis Project. *Bull. Amer. Meteor. Soc.*, **77**, 437–471, doi:10.1175/1520-0477(1996)077<0437:TNYRP>2.0.CO;2.

Kundu, P. K., and J. P. McCreary, 1986: On the dynamics of the throughflow from the Pacific into the Indian Ocean. *J. Phys. Oceanogr.*, **16**, 2191–2198, doi:10.1175/1520-0485(1986)016<2191:OTDOTT>2.0.CO;2.

Lambert, E., D. Le Bars, and W. P. M. de Ruijter, 2016: The connection of the Indonesian Throughflow, South Indian Ocean Countercurrent and the Leeuwin Current. *Ocean Sci.*, **12**, 771–780, doi:10.5194/os-12-771-2016.

Maltrud, M. E., R. D. Smith, A. J. Semtner, and R. C. Malone, 1998: Global eddy-resolving ocean simulation driven by 1985–1995 atmospheric winds. *J. Geophys. Res.*, **103**, 30 825–30 853, doi:10.1029/1998JC900013.

Marchuk, G. I., A. J. Sarkisian, and V. P. Kochergin, 1973: Calculations of flows in a baroclinic ocean: Numerical methods and results. *Geophys. Astrophys. Fluid Dyn.*, **5**, 89–99, doi:10.1080/03091927308236109.

Masumoto, Y., and Coauthors, 2004: A fifty-year eddy-resolving simulation of the world ocean: Preliminary outcomes of OFES (OGCM for the Earth Simulator). *J. Earth Simul.*, **1**, 35–56. [Available online at http://www.jamstec.go.jp/esc/publication/journal/jes_vol.1/pdf/JES1-3.2-masumoto.pdf.]

Maximenko, N., O. V. Melnichenko, P. P. Niller, and H. Sasaki, 2008: Stationary mesoscale jet-like features in the ocean. *Geophys. Res. Lett.*, **35**, L08603, doi:10.1029/2008GL033267.

——, P. Niiler, M.-H. Rio, O. Melnichenko, L. Centurioni, D. Chambers, V. Zlotnicki, and B. Galperin, 2009: Mean dynamic topography of the ocean derived from satellite and drifting buoy data using three different techniques. *J. Atmos. Oceanic Technol.*, **26**, 1910–1919, doi:10.1175/2009JTECHO672.1.

McCreary, J. P., S. R. Shetye, and P. K. Kundu, 1986: Thermohaline forcing of eastern boundary currents: With application to the circulation off the west coast of Australia. *J. Mar. Res.*, **44**, 71–92, doi:10.1357/002224086788460184.

——, P. K. Kundu, and S.-Y. Chao, 1987: On the dynamics of the California Current System. *J. Mar. Res.*, **45**, 1–32, doi:10.1357/002224087788400945.

Menezes, V. V., H. E. Phillips, A. Schiller, C. M. Domingues, and N. L. Bindoff, 2013: Salinity dominance on the Indian Ocean Eastern Gyral Current. *Geophys. Res. Lett.*, **40**, 5716–5721, doi:10.1002/2013GL057887.

——, ——, ——, N. L. Bindoff, C. M. Domingues, and M. L. Vianna, 2014: South Indian Countercurrent and associated fronts. *J. Geophys. Res. Oceans*, **119**, 6763–6791, doi:10.1002/2014JC010076.

Meuleners, M. J., C. B. Pattiaratchi, and G. N. Ivey, 2007: Numerical modelling of the mean flow characteristics of the Leeuwin Current System. *Deep-Sea Res. II*, **54**, 837–858, doi:10.1016/j.dsr2.2007.02.003.

——, G. N. Ivey, and C. B. Pattiaratchi, 2008: A numerical study of the eddying characteristics of the Leeuwin Current System. *Deep-Sea Res. I*, **55**, 261–276, doi:10.1016/j.dsr.2007.12.004.

Meyers, G., R. J. Bailey, and A. P. Worby, 1995: Geostrophic transport of Indonesian Throughflow. *Deep-Sea Res. I*, **42**, 1163–1174, doi:10.1016/0967-0637(95)00037-7.

Middleton, J. F., and M. Cirano, 2002: A northern boundary current along Australia's southern shelves: The Flinders Current. *J. Geophys. Res.*, **107**, 3129, doi:10.1029/2000JC000701.

Mountain, D. G., 1974: Preliminary analysis of Beaufort shelf circulation in summer. *The Coast and Shelf of the Beaufort Sea: Proceedings of a Symposium on Beaufort Sea Coast and Shelf Research*, J. C. Reed and J. E. Sater, Eds., Arctic Institute of North America, 27–48.

Nakano, H., and H. Hasumi, 2005: A series of zonal jets embedded in the broad zonal flows in the Pacific obtained in eddy-permitting ocean general circulation models. *J. Phys. Oceanogr.*, **35**, 474–488, doi:10.1175/JPO2698.1.

National Geographical Data Center, 1988: Data announcement 88-MGG-02: Digital relief of the surface of the earth. NOAA/National Geophysical Data Center, 2 pp.

Oke, P. R., and Coauthors, 2013: Evaluation of a near-global eddy-resolving ocean model. *Geosci. Model Dev.*, **6**, 591–615, doi:10.5194/gmd-6-591-2013.

Palastanga, V., P. J. van Leeuwen, M. W. Schouten, and W. P. M. de Ruijter, 2007: Flow structure and variability in the subtropical Indian Ocean: Instability of the South Indian Ocean Countercurrent. *J. Geophys. Res.*, **112**, C01001, doi:10.1029/2005JC003395.

Pearce, A., and C. B. Pattiaratchi, 1999: The Capes Current: A summer countercurrent flowing past Cape Leeuwin and Cape Naturaliste, Western Australia. *Cont. Shelf Res.*, **19**, 401–420, doi:10.1016/S0278-4343(98)00089-2.

Qiu, B., D. L. Rudnick, S. Chen, and Y. Kashino, 2013: Quasi-stationary North Equatorial Undercurrent jets across the tropical North Pacific Ocean. *Geophys. Res. Lett.*, **40**, 2183–2187, doi:10.1002/grl.50394.

Rennie, S. J., C. B. Pattiaratchi, and R. D. McCauley, 2007: Eddy formation through the interaction between the Leeuwin Current, Leeuwin Undercurrent and topography. *Deep-Sea Res. II*, **54**, 818–836, doi:10.1016/j.dsr2.2007.02.005.

Reynolds, R. W., T. M. Smith, C. Liu, D. B. Chelton, K. S. Casey, and M. G. Schlax, 2007: Daily high-resolution-blended analyses for sea surface temperature. *J. Climate*, **20**, 5473–5496, doi:10.1175/2007JCLI1824.1.

Ridgway, K. R., and J. R. Dunn, 2003: Mesoscale structure of the mean East Australian Current System and its relationship with topography. *Prog. Oceanogr.*, **56**, 189–222, doi:10.1016/S0079-6611(03)00004-1.

——, and J. Godfrey, 2015: The source of the Leeuwin Current seasonality. *J. Geophys. Res. Oceans*, **120**, 6843–6864, doi:10.1002/2015JC011049.

——, J. R. Dunn, and J. L. Wilkin, 2002: Ocean interpolation by four-dimensional weighted least squares—Application to the waters around Australasia. *J. Atmos. Oceanic Technol.*, **19**, 1357–1375, doi:10.1175/1520-0426(2002)019<1357:OIBFDW>2.0.CO;2.

Sælen, O. H., 1959: Preliminary report on the hydrographic sections made in the Norwegian Sea 1958 by Geofysisk Institutt, Bergen. Special IGY Meeting ICES CM Doc. 46, 6 pp. [Available online at http://hdl.handle.net/11250/101261.]

Sasaki, H., M. Nonaka, Y. Masumoto, Y. Sasai, H. Uehara, and H. Sakuma, 2008: An eddy-resolving hindcast simulation of the quasiglobal ocean from 1950 to 2003 on the Earth Simulator. *High Resolution Numerical Modelling of the Atmosphere and Ocean*, K. Hamilton and W. Ohfuchi, Eds., Springer, 157–185.

Saville-Kent, W., 1897: *The Naturalist in Australia*. Chapman & Hall, 302 pp.

Schott, F. A., S.-P. Xie, and J. P. McCreary, 2009: Indian Ocean circulation and climate variability. *Rev. Geophys.*, **47**, RG1002, doi:10.1029/2007RG000245.

Sheng, J., and K. R. Thompson, 1996: A robust method for diagnosing regional shelf circulation from scattered density profiles. *J. Geophys. Res.*, **101**, 25 647–25 659, doi:10.1029/96JC01331.

Siedler, G., M. Rouault, and J. R. E. Lutjeharms, 2006: Structure and origin of the subtropical South Indian Ocean Countercurrent. *Geophys. Res. Lett.*, **33**, L24609, doi:10.1029/2006GL027399.

Smith, R. L., A. Huyer, J. S. Godfrey, and J. A. Church, 1991: The Leeuwin Current off Western Australia, 1986–1987. *J. Phys. Oceanogr.*, **21**, 323–345, doi:10.1175/1520-0485(1991)021<0323:TLCOWA>2.0.CO;2.

Taguchi, B., R. Furue, N. Komori, A. Kuwano-Yoshida, M. Nonaka, H. Sasaki, and W. Ohfuch, 2012: Deep oceanic zonal jets constrained by fine-scale wind stress curls in the South Pacific Ocean: A high-resolution coupled GCM study. *Geophys. Res. Lett.*, **39**, L08602, doi:10.1029/2012GL051248.

Thompson, R. O. R. Y., 1984: Observations of the Leeuwin Current off Western Australia. *J. Phys. Oceanogr.*, **14**, 623–628, doi:10.1175/1520-0485(1984)014<0623:OOTLCO>2.0.CO;2.

——, 1987: Continental-shelf-scale model of the Leeuwin Current. *J. Mar. Res.*, **45**, 813–827, doi:10.1357/002224087788327190.

Weaver, A. J., and J. H. Middleton, 1989: On the dynamics of the Leeuwin Current. *J. Phys. Oceanogr.*, **19**, 626–648, doi:10.1175/1520-0485(1989)019<0626:OTDOTL>2.0.CO;2.

——, and ——, 1990: An analytic model for the Leeuwin Current off West Australia. *Cont. Shelf Res.*, **10**, 105–122, doi:10.1016/0278-4343(90)90025-H.

Wijffels, S. E., G. Meyers, and J. S. Godfrey, 2008: A 20-yr average of the Indonesian Throughflow: Regional currents and the interbasin exchange. *J. Phys. Oceanogr.*, **38**, 1965–1978, doi:10.1175/2008JPO3987.1.

Woo, L. M., and C. B. Pattiaratchi, 2008: Hydrography and water masses off the western Australian coast. *Deep-Sea Res. I*, **55**, 1090–1104, doi:10.1016/j.dsr.2008.05.005.

——, ——, and W. W. Schroeder, 2006: Dynamics of the Ningaloo Current off Point Cloates, Western Australia. *Mar. Freshwater Res.*, **57**, 291–301, doi:10.1071/MF05106.

Yit Sen Bull, C., and E. van Sebille, 2016: Sources, fate, and pathways of Leeuwin Current water in the Indian Ocean and Great Australian Bight: A Lagrangian study in an eddy-resolving ocean model. *J. Geophys. Res. Oceans*, **121**, 1626–1639, doi:10.1002/2015JC011486.